

Chapter 2

The Advanced Accumulator: A New Passive ECCS Component of the APWR

Tadashi Shiraishi

With the increased requirement for nuclear power generation as an effective countermeasure against global warming, Mitsubishi has developed the advanced pressurized water reactor (APWR) by adopting a new component of the emergency core cooling system (ECCS), a new instrumentation and control system, and other newfound improvements. The ECCS introduces a new passive component called the Advanced Accumulator which integrates both functions of the conventional accumulator and the low-pressure pump without any moving parts. The Advanced Accumulator uses a new fluidics device that automatically controls flow rates of injected water in case of a loss-of-coolant accident (LOCA). This fluidics device is referred to as a flow damper. In this chapter, the Advanced Accumulator is introduced from the background of its development to its principle, with some experimental results. Furthermore, the features of the flow damper are explained in detail.

2.1 Overview of the APWR

The development of the APWR was launched jointly by the Japanese government, five utility companies (Hokkaido Electric Power Co., Kansai Electric Power Co., Shikoku Electric Power Co., Kyushu Electric Power Co., and Japan Atomic Power Company) and suppliers, including Mitsubishi, in the early 1980s, under the Third Phase Improvement Standardization Program for Light Water Reactors [1]. The development was aimed at establishing an advanced standard light-water reactor with further enhanced reliability and safety, improved economy and more efficient usage of location with increased power, based on the results of the First and Second Phase Improvement Standardization Programs. The development also involved Mitsubishi's experience and technologies obtained through the design, construction,

T. Shiraishi (✉)
Mitsubishi Heavy Industries, Ltd, Tokyo, Japan
e-mail: tadashi_shiraishi@mhi.co.jp

and operation of existing PWR plants. Even after the completion of the national programs, under the continuous support of the utilities, the APWR design has been improved through uprating by redesigning its core structure, optimizing its safety systems by introducing an advanced accumulator tank, and making other modifications. In March 2004, the Japan Atomic Power Company applied for the approval of changes in the reactor installation related to the addition of Tsuruga Units 3 and 4, the first two APWRs. As a result, the government has started the safety assessment of these units.

On the basis of the operating success of these units, Mitsubishi is making efforts to establish APWRs as a lineup of large-capacity standard PWR plants with excellent enhanced economy. This lineup includes 1,600 and 1,700 MWe class APWRs whose design certification in the US has already been applied for, with high-performance steam generators and steam turbines. The APWRs have realized a large capacity increase of about 30% or more, compared with the current 4-loop PWRs as shown in Fig. 2.1.

The main features of APWR plant components, as outlined in this section, are as follows:

1. Large reactor core and main components with large capacity (steam generator, primary coolant pump, pressurizer, and turbine)

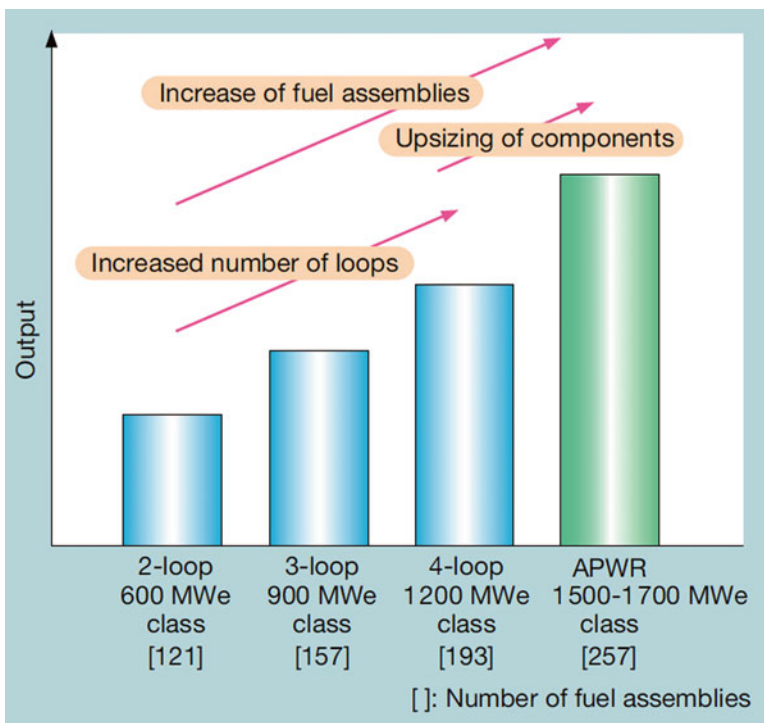


Fig. 2.1 The trend in output capacity of PWR plants

2. Advanced safety systems (four subsystems and refueling water storage pit installed in the reactor containment)
3. New instrumentation and control systems (advanced digital main control board)

2.1.1 Large Capacity Core

The APWR has adopted a large capacity core to achieve high thermal power and has increased the number of fuel assemblies from 193 in the current 4-loop type to 257 as shown in Fig. 2.2. An advanced 17×17 fuel assembly has been adopted as the fuel bundle, and also, a zircaloy grid that absorbs fewer neutrons, which is already used in current plants, has been incorporated for the effective use of uranium resources. Furthermore, the APWR allows the number of control rods to be set according to the quantity of loaded MOX fuel, so that the requirement for diverse operations, such as the use of a MOX core and high burnup, can be met flexibly.

2.1.2 Neutron Reflector

The APWR employs a neutron reflector as an internal component for effective use of uranium resources. The reflector has a simple structure that consists of stacked blocks of stainless steel rings without weld lines and with a few bolt connections, whereas the same internal in the current PWR has a baffle structure in which stainless steel plates are connected with many bolts as shown in Fig. 2.3. The new structure reduces neutron irradiation to the reactor vessel to about 1/3 so that the reliability of the vessel is improved.

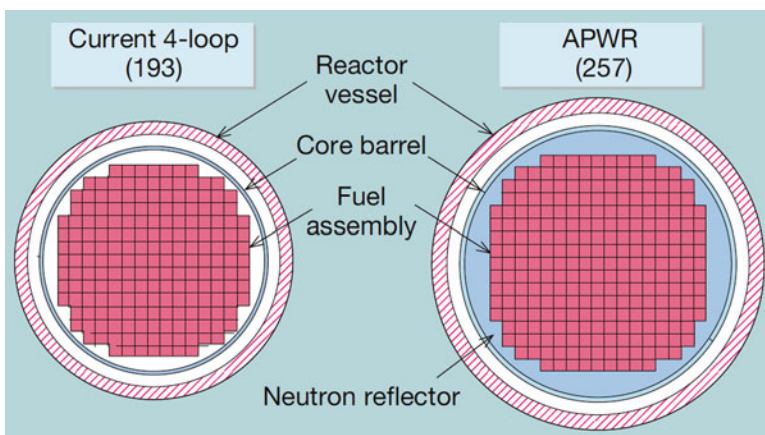


Fig. 2.2 The APWR adopts a larger core to increase the number of fuel assemblies from 193 to 257

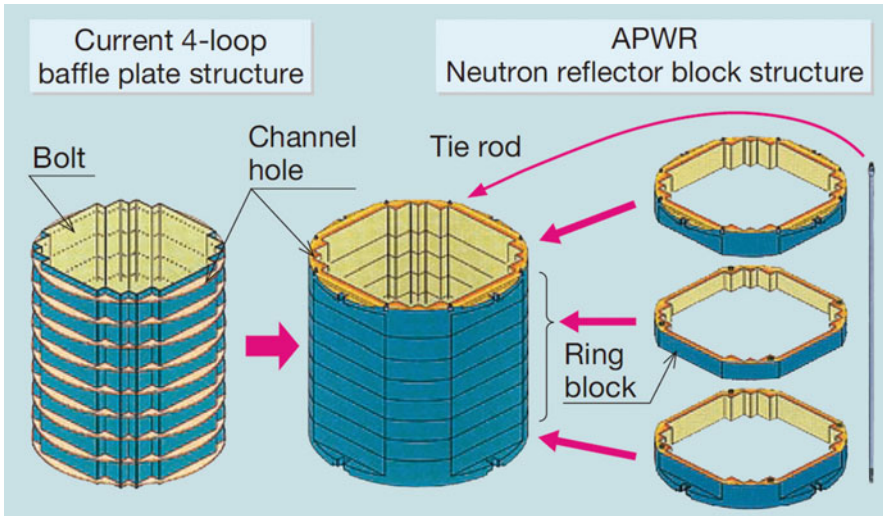


Fig. 2.3 The neutron reflector for the APWR consists of rings without weld lines and with only a few bolt connections

2.1.3 Advanced Safety Systems

In the APWR, the emergency core cooling system (ECCS) has a 4-train configuration ($4 \times 50\%$ capacity) instead of the conventional 2-train configuration ($2 \times 100\%$ capacity) to improve safety. The new configuration increases the reliability of equipment operation in the case of an accident as the best mix of active and passive safety systems. The systems of each train are installed near the corresponding loop to reduce the quantity of piping and enhance the separation and independence of each train. A refueling water storage pit is moved from outside of the containment vessel to the bottom of the vessel to serve as a water source for the ECCS during an accident. With this design, cooling water injected into the core during an accident can be automatically collected in the pit. This eliminates the changeover operation of the core cooling water source and enhances safety. Furthermore, an Advanced Accumulator with a passive concept has been adopted. It is explained in detail in this chapter.

2.1.4 Advanced Main Control Board and Integrated Digital Control and Protection System

Compact console panels are adopted in the advanced main control board to accomplish all monitoring and operations by touch screen displays. The operational



Fig. 2.4 Advanced main control board (prototype)

switches of the plant components and the necessary operation information are consolidated on the screen to improve the operators' performance as shown in Fig. 2.4. When an anomaly occurs in the plant, the panel's rich supporting functions automatically check the status of the plant and equipment operation and provide the necessary information. Compared with the conventional type, the advanced main control board is expected to reduce the operators' burden by about 30% and human error by about 50%.

2.1.5 Main Components with Increased Capacity

Main components with increased capacity have been developed to cope with the increased core output, and various technologies to improve performance and reliability are being adopted and verified. According to the lineup of plant electricity output, a compact, high-performance steam generator (SG) with a substantially larger heat transfer area than that of the conventional 4-loop type is employed as shown in Fig. 2.5. In order to minimize the increase of the outer dimensions of the increased capacity SG, the tube diameter has been decreased from 7/8 to 3/4 inches to reduce the diameter of the SG, and an improved moisture separator with a reduced number of stages has been adopted to reduce the SG height. This reduces the weight of the SG by about 10% or more compared with the larger SG based on the conventional design concept. To improve reliability, the number of antivibration bars installed at U-bends has been increased from six in the current plants to nine or more.

To provide high efficiency to the steam turbine, the last-stage blades of the low pressure turbine have been extended by adopting blades as long as 54–74 in. Ideal

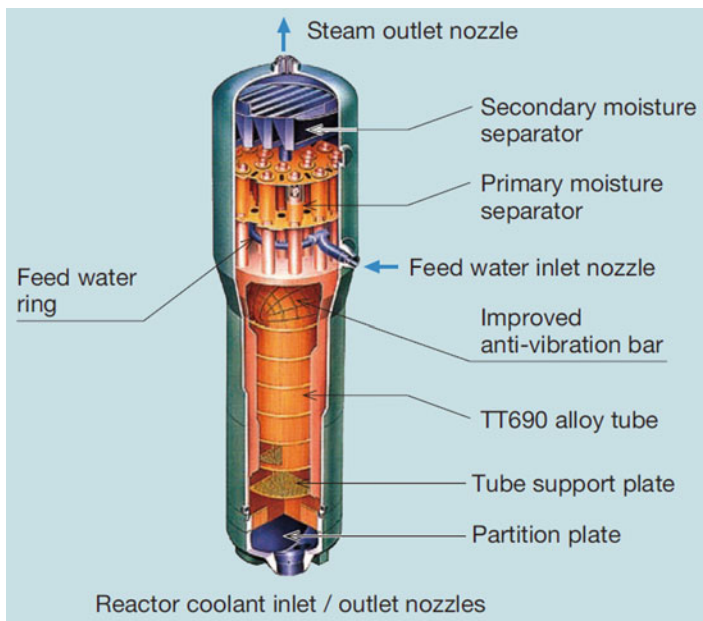


Fig. 2.5 The compact, high-performance steam generator for the APWR has a large heat transfer area in a minimized size

high-performance three-dimensional (3D) blades have been adopted to reduce blade loss by making a complete 3D flow design. Furthermore, integral shroud blades (ISBs) aimed at reducing vibration stress by forming an all-round stitch structure through contact with adjacent blades during revolution have also been adopted to enhance reliability. The developed blades were tested under actual steam conditions at Mitsubishi's own test facility, the world's largest class test facility, to verify their performance and reliability as shown in Fig. 2.6. These new technologies are also being applied in the replacement of turbines in existing domestic and overseas plants.

2.2 Development of the Advanced Accumulator

Globally speaking, development of passive safety systems for nuclear plants thrived in the 1980s against the backdrop of the Three-mile Island Accident in March of 1979 and the Chernobyl Accident in April of 1986. At the time, Mitsubishi Heavy Industries, Ltd. (MHI) had been developing a hybrid safety system, namely, orchestrating the merits of both passive and active safety systems [2]. The designers of the hybrid safety system requested the members of the R&D group to propose a device that changes the flow rate of the ECCS with high reliability and is maintenance-free for the plant life time. The solution we proposed was the Advanced Accumulator with a new fluidics device, called a flow damper which

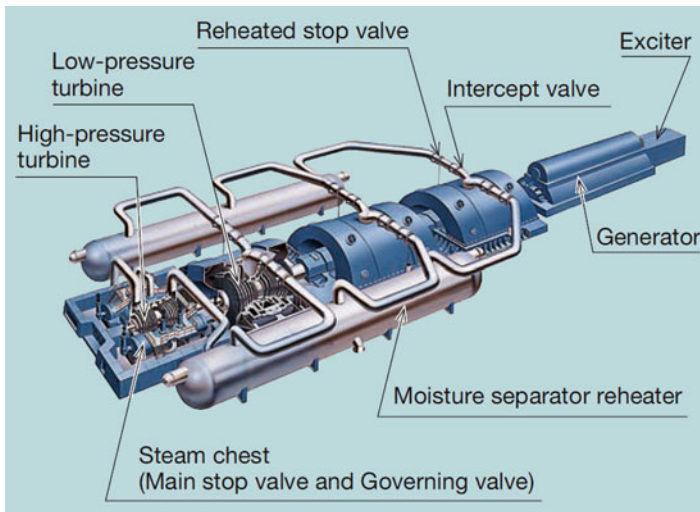


Fig. 2.6 Large-capacity, high-performance turbine generator system

has no moving parts. Since there are no moving parts, fluidic elements have extraordinary reliability and require no maintenance.

The Advanced Accumulator was invented using the science of fluidics in 1986 [3] and was developed for Mitsubishi's next generation PWR after the APWR from 1987 to 1994. The experimental results were reported in [4–10]. The results were successful in that the Advanced Accumulator was experimentally verified to have the basic functions that we expected, and the ratio of flow rates for large and small flow injections was confirmed to satisfy the requirement for the next generation PWR.

The development of the Advanced Accumulator for the APWR was then initiated in 1995 and completed in 1997. Since a fluidic element has no moving parts, its configuration had to be modified for different specifications. The Advanced Accumulator for the APWR was incorporated into the safety system design to provide the low-pressure injection function of the current ECCS using a conventional accumulator and a safety injection pump. This arrangement simplifies the configuration of ECCS and allows sufficient time to use gas-turbine generators for safety injection pumps.

2.3 ECCS of the APWR

A loss of coolant accident (LOCA) is the severest hypothetical accident. Figure 2.7 shows the scenario of a large break LOCA of PWR as follows:

1. One of the main coolant pipes is assumed to break with a large opening.
2. Pressure in the reactor vessel plummets towards atmospheric pressure.

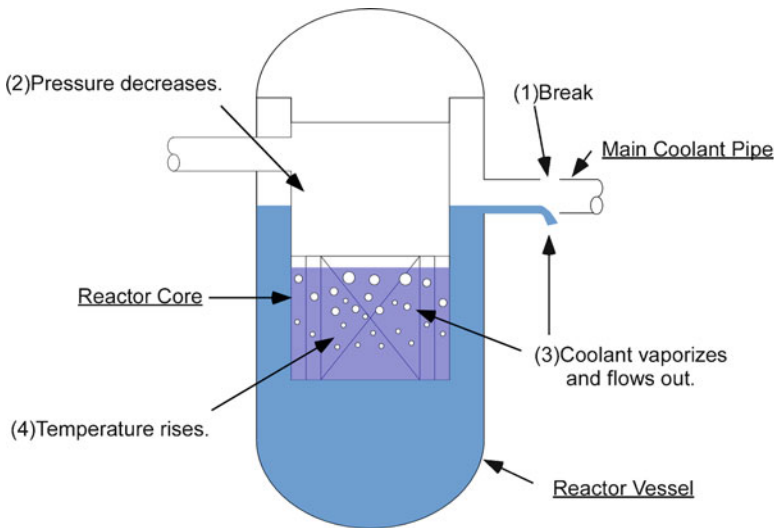


Fig. 2.7 At a large break LOCA, one of the main coolant pipes is assumed to break with a large opening. The coolant will then vaporize and flow out of the main coolant pipe

3. Coolant vaporizes in the reactor vessel and flows out the opening of the main coolant pipe to expose the reactor core.
4. The fuel cladding temperature begins to rise and requires additional coolant to protect fuels from serious damage.

The ECCS supplies boric acid water into the reactor vessel to meet the requirement of sufficient cooling of the reactor core at LOCA. Figure 2.8 compares the ECCS configurations of the current 4-loop PWR and APWR. The current 4-loop PWR has two trains of injection systems, conventional accumulators, and a refueling water storage pit outside of the containment vessel. The APWR has some improvements, which include the following:

1. Four trains of the injection system composed of simplified pipe routing for higher reliability
2. Four Advanced Accumulators that allow for the elimination of low-head safety injection pumps
3. An in-containment refueling water storage pit located in the containment vessel for higher reliability

Thus, the current ECCS is composed of the accumulator injection system with conventional accumulators, a low-head injection subsystem, and a high-head injection subsystem. The new ECCS for APWR is composed of the accumulator injection system with Advanced Accumulators and a safety injection subsystem without low-head safety injection pumps.

Figure 2.9 shows a view of the safety system of APWR. There is a reactor vessel (2) at the center of the containment vessel (1), to which steam generators (3) and

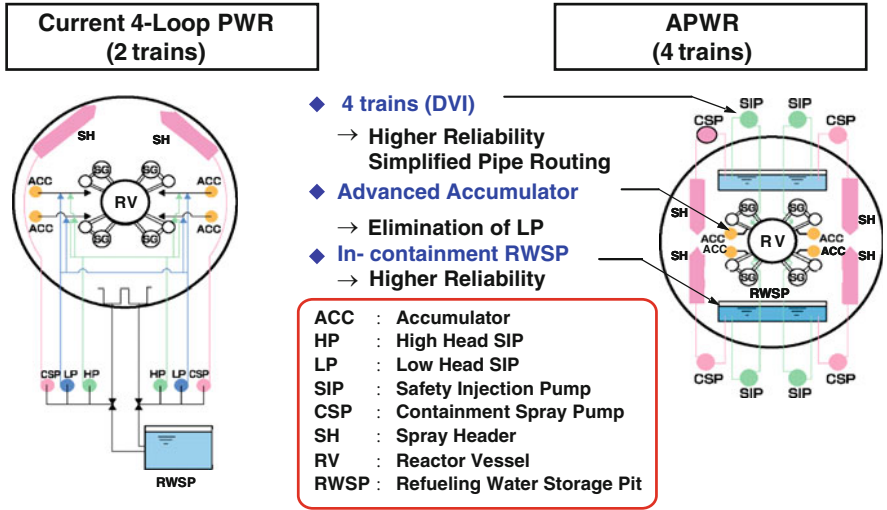


Fig. 2.8 Configurations of the ECCS for the current 4-loop PWR and APWR. The APWR has higher reliability and a simplified pipe routing without low-head injection pumps. The systems of each train are installed near the corresponding loop to reduce the quantity of piping and enhance the train separation and independence

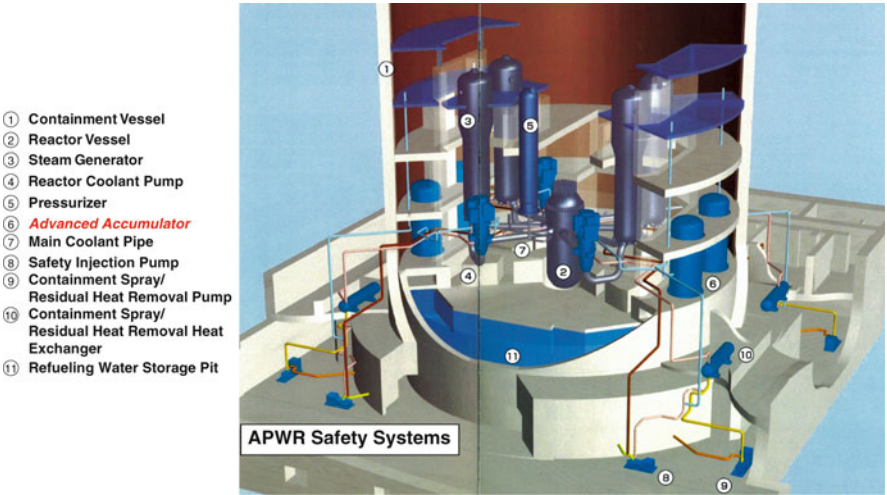


Fig. 2.9 Cut-away view of the safety system of the APWR shows the configuration of the components

reactor coolant pumps (4) are connected by the main coolant pipes (7) to form loops. A pressurizer (5) is connected to one of the loops. An Advanced Accumulator (6) is connected to every main coolant pipe (7). Safety injection pumps (8) are located outside of the containment vessel. Containment spray/residual heat removal

pumps (9), heat exchangers (10), and a refueling water storage pit (11) compose the residual heat removal system located outside of the containment vessel. Each train of the ECCS has one Advanced Accumulator and one safety injection pump, and it is connected to the common refueling water storage pit.

Borated water injection by the ECCS for PWRs has three steps after blow down due to a large break LOCA.

Step 1: *Core Refilling* injects water rapidly at a large flow rate to fill the lower plenum and downcomer of the reactor vessel in a short time.

Step 2: *Core Reflooding* recovers the core water level using the water head in the downcomer. ECCS injection keeps the high water level in the downcomer and immediately re-floods the core.

Step 3: *Long-Term Cooling* injects water to compensate for water reduction due to evaporation by decay heat and maintains a reflooded condition of the core after core reflooding is completed.

The requirement for injection of borated water varies at every step as shown in Fig. 2.10. If a large break LOCA happens, a large flow rate of injected water is required at Step 1 for Core Refilling. The water head in the downcomer drives water into the reactor core at Step 2 for Core Reflooding. At this step, a relatively small flow rate is required because any excess water will flow out of the opening to no purpose. The reactor core will be covered with water at the end of the Core Reflooding and Step 3 starts for Long-Term Cooling.

The current 4-loop plants satisfy the requirement of flow rate by conventional accumulators at Step 1, and by low-head and high-head injection pumps at Steps 2 and 3. Each conventional accumulator injects borated water using the pressure of

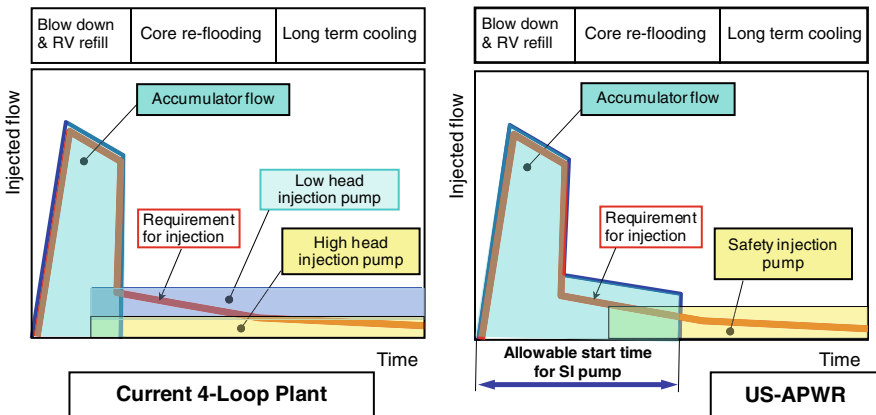


Fig. 2.10 The schematic drawings on the *left* and the *right* show the injection modes of the current 4-loop plant and of the APWR, respectively. The APWR is improved by using the Advanced Accumulators to eliminate the low-head injection pumps and to obtain a longer allowable start time for SI pumps

nitrogen gas stored in it, while low-head and high-head injection pumps are driven by diesel generators.

On the contrary, the APWR satisfies the requirement by the Advanced Accumulators at Steps 1 and 2, and by Safety Injection Pumps at Step 3. The advantages of the Advanced Accumulators are the automatic changeover of injected flow rate from Step 1 to Step 2 in the absence of moving parts, and eliminating the low-head injection subsystem. Each Advanced Accumulator injects borated water using the pressure of stored nitrogen gas, the same as the conventional accumulators do. Furthermore, longer time injection of the Advanced Accumulators allows a longer time to prepare for the start of the safety injection pumps. In other words, not only diesel generators but also gas-turbine generators can be selected for the safety injection pumps.

2.4 Characteristics of the Advanced Accumulator

The configurations of the current and new safety systems are shown in Fig. 2.11. The current safety system is composed of conventional accumulators, low-head injection pumps and high-head injection pumps, which are not shown within the figure. The new safety system is composed of Advanced Accumulators and safety injection pumps, which are also not represented within the figure. The Advanced Accumulator has a flow damper at the bottom of the tank. The Advanced Accumulator orchestrates large flow injection for refilling and small flow injection for

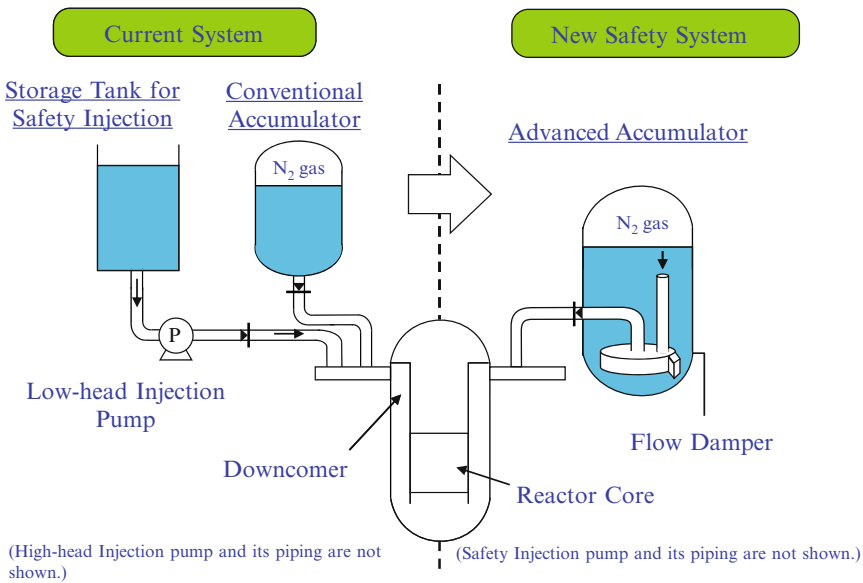


Fig. 2.11 The current safety system has a low-head injection system in addition to a conventional accumulator, while the new safety system has an Advanced Accumulator

reflooding. Since the low-head injection pumps are not needed, that allows a longer time to start the safety injection pumps.

Both conventional and Advanced Accumulators drive borated water with nitrogen gas filled at the tops of their tanks. There is a standpipe which detects water level in the tank of the Advanced Accumulator. The standpipe is connected to the large flow pipe of the flow damper to supply water only for large flow injection. Stopping the supply of flow from the standpipe changes the flow resistance of the flow damper without using moving parts.

Figure 2.12 shows the specific configuration of the ECCS for the APWR. Four Advanced Accumulators are installed and each Advanced Accumulator connects to a separate cold leg of the reactor coolant system (RCS). Four high-head safety injection subsystems are installed in order to inject water following injection by the Advanced Accumulators. There is no low-head injection subsystem.

The fundamental safety requirement for the ECCS is to limit the peak clad temperature (PCT) of fuel rods in the reactor core to 1,200°C during a large break

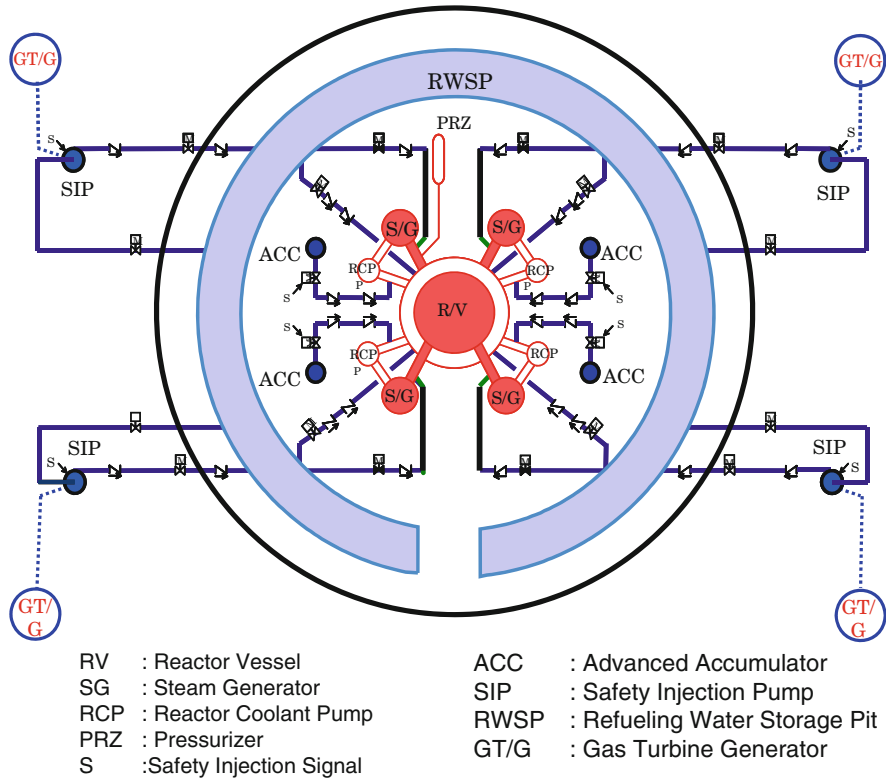


Fig. 2.12 The ECCS of the APWR has four pipelines for the safety injection pumps. Each Advanced Accumulator is connected to a separate cold leg. The refueling water storage pit is placed at the *bottom* of the containment vessel

LOCA. The functions of the Advanced Accumulators are encompassed within the following two steps:

1. To immediately refill the lower plenum and the downcomer of the reactor vessel during refilling period following blow down of reactor coolant
2. To establish a reflooding condition of the core by maintaining the water level in the downcomer after refilling the core

Hence, the performance requirements for the Advanced Accumulator design are the requirements for large flow injection, which comes from Step 1, and for small flow injection which comes from Step 2.

The requirements for large flow injection during the refilling period are that the water volume for large flow injection in the accumulator tank should cover the total volume of the lower plenum and downcomer regions of the reactor vessel, and that the lower plenum and the downcomer should be filled with borated water as rapidly as possible during the refilling period. The requirements for small flow injection are that the required small injected flow rate is determined by the performance requirements of the ECCS, along with the assumption that 3-out-of-4 sets of Advanced Accumulators are available. The large injected flow rate before flow-rate change-over is given by the expected flow rate at the end of large flow injection from calculated results. Consequently, the requirement for the flow-rate changeover ratio from large to small flow injection should be less than the maximum value required for small injected flow rate and be set with some margin.

2.5 Development of the Advanced Accumulator

The functions of the Advanced Accumulator are realized by a new fluidics device called a flow damper. It secures the large flow injection, the rapid flow changeover, the desired ratio of injected flow rates before and after the changeover, and the small flow injection. The flow damper is named after its function to restrict flow.

2.5.1 *Structure of the Flow Damper*

Figure 2.13 shows the structure of the flow damper and its installation at the bottom of the accumulator tank. There is a vortex chamber at the center of the flow damper. A small flow pipe is tangentially attached to the vortex chamber. A large flow pipe is radially attached to the chamber at one end and is connected to the standpipe at the other end. An outlet nozzle stands at the center of the vortex chamber, and is connected to the outlet pipe which leads to the injection pipe. An antivortex cap and an antivortex plate are set on the upper inlet of the standpipe and the lower inlet of the small flow pipe, respectively.

The antivortex cap installed on the inlet port of the standpipe prevents the formation of a vortex and gas entrainment in the flow damper just before the flow changeover. Additionally, it improves flow-rate changeover characteristics.

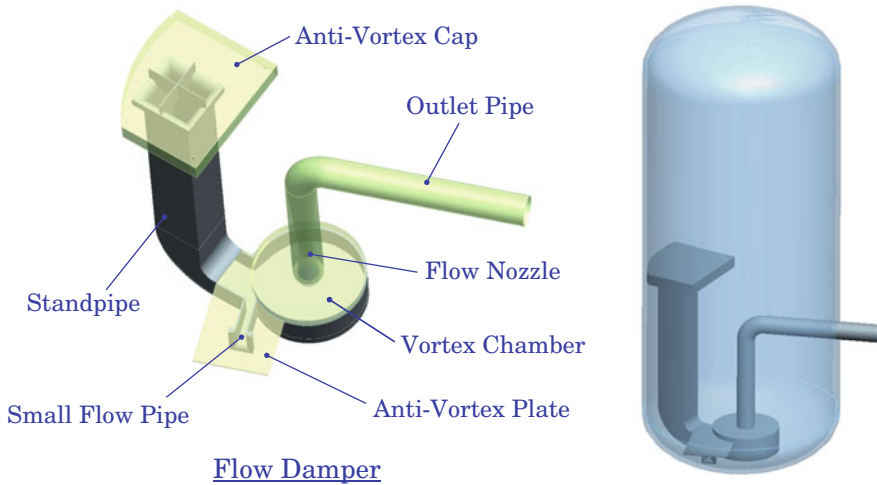


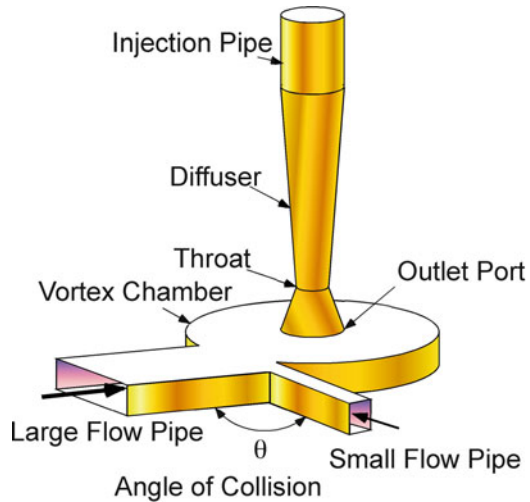
Fig. 2.13 Schematic views of the flow damper. Its detailed structure appears on the *left* and its installation in the accumulator tank is shown on the *right*

The inlet of the standpipe is set at the water level for switching flow from large to small flow injections. The small flow pipe is tangentially attached to the vortex chamber and has a configuration designed to reduce energy loss in it to make a strong vortex in the chamber. A throat is provided to increase flow resistance during small flow injection along with a diffuser to recover pressure during large flow injection in the outlet nozzle, which is smoothly connected to the injection pipe. The injection pipe is connected to a cold leg of the RCS. The antivortex plate on the small flow pipe prevents gas entrainment at the very last time of small flow injection.

2.5.2 Design of the Flow Damper

The mechanical configuration of the flow damper is shown in Fig. 2.14. The vortex chamber is chosen to be a cylindrical structure able to form a strong vortex in it. The small flow pipe is tangentially connected to the vortex chamber to yield a strong vortex for small flow injection. If energy loss is negligible in the chamber, the angular momentum is preserved to form a free vortex. The formation of a free vortex is very useful to get a large pressure drop across the vortex chamber. The pressure drop will be larger as the ratio of the radii of the chamber and the throat gets larger. But a larger ratio of the radii requires a larger space for the vortex chamber. Therefore, the optimum ratio for the radii will be achieved based on the required characteristics of the flow damper and the space in which the flow damper can be placed. The ratio of the radii is one of the key parameters of the flow damper. The vortex may be so strong that cavitation could appear at the center of the vortex

Fig. 2.14 Mechanical configuration of the flow damper. It consists of large and small flow pipes, a vortex chamber, and an outlet nozzle, which is composed of a reducer, a throat, and a diffuser. The reducer is between the outlet port and the throat



chamber. The reducer between the outlet port of the vortex chamber and the throat prevents the influence of cavitation on the flow and stabilizes the flow in it. Large energy loss occurs in the strong shear layer at the center of the vortex core and in the diffuser. Most of the energy is lost before the exit of the diffuser.

The large flow pipe is radially connected to the vortex chamber at a certain angle to cancel out the vortex formed by flow from the small flow pipe during large flow injection. The angle of collision of the large to small flows is one of the key parameters for the flow damper design. The width of the large flow pipe is set as large as possible to get a large ratio of flow rates. The detailed design of the configuration at the inlet ports of the large and small flow pipes will be one of the key items to get good characteristics of the flow damper. The reducer upstream from the throat prevents or minimizes the separation of flow at the exit of the outlet port and stabilizes the flow at the throat. The diffuser downstream from the throat will recover the static pressure during large flow injection. The size of the throat is determined by the required flow rate during large flow injection. The other dimensions can be determined by the size of the throat in a similar manner as the configuration of the flow damper model for which flow characteristics were investigated.

2.5.3 Principle of the Advanced Accumulator

Figure 2.15 shows the configurations and the principle of the Advanced Accumulator. The flow damper is installed at the bottom of the accumulator tank as shown in Fig. 2.15a, the center drawing. The lower inlet port of the small flow pipe is on the same level as the vortex chamber at the bottom of the tank. The standpipe is connected

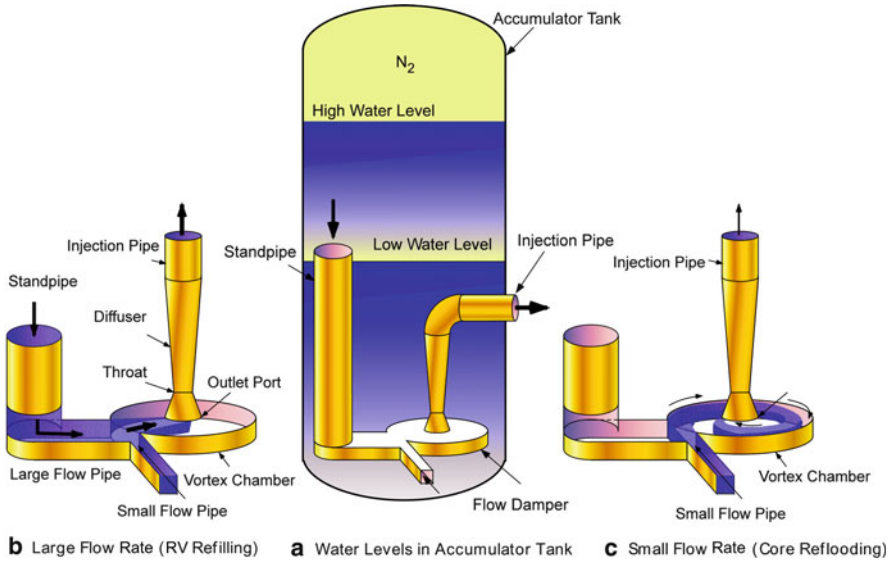


Fig. 2.15 The principle of the Advanced Accumulator showing flow patterns depending on the water level in the accumulator tank

to the large flow pipe. The inlet port of the standpipe is located at the middle level of the accumulator tank where there is a boundary between the large and small flow volumes. The outlet pipe is connected to the injection pipe at the boundary of the wall of the accumulator tank. The antivortex cap and plate are not illustrated in the figure for simplicity.

Initially, the water level in the accumulator tank is high above the inlet port of the standpipe. Once injection starts at a large break LOCA, water comes into both the upper and lower inlet ports, and the water level comes down. The flows from both of the inlets collide with each other and do not form a vortex in the vortex chamber as shown in Fig. 2.15b. Thus, the flow resistance of the flow damper comes from only the form resistance which is relatively small. A large flow rate is then obtained.

After the water level falls below the upper inlet port of the standpipe, water stops flowing into the standpipe. The other flow in the small flow pipe forms a strong and steady vortex in the vortex chamber as shown in Fig. 2.15c. Thus, the flow resistance of the flow damper comes from the strong and large vortex. The small flow rate is then achieved.

Consequently, the standpipe detects the water level at which flow rate must be changed, and formation of a strong vortex in the chamber reduces the flow rate in the absence of any moving parts. The accumulator tank should have the total capacity to accommodate the nitrogen gas, and large and small coolant flow volumes.

Figure 2.16 shows an example of flow rate transition of the Advanced Accumulator. As the injection starts, the flow rate goes to its maximum, and gradually falls due to

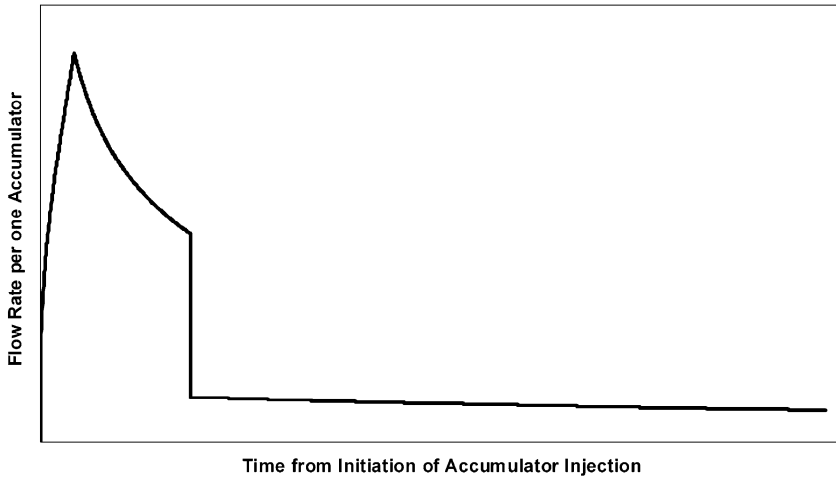


Fig. 2.16 An example of flow rate transition of the Advanced Accumulator. The flow rate is quickly changed from large flow injection to small flow injection

the pressure drop of nitrogen gas expansion. This is the large flow injection. At the time of flow changeover, the flow rate quickly switches and keeps small flow injection with a small decrease. This is the small flow injection.

2.5.4 Theoretical Consideration of the Flow Damper

For large flow injection, total angular momentum of flows from the large and small flow pipes must be zero. Furthermore, the resultant conflux must go straight to the outlet port of the vortex chamber in order not to form a vortex in the vortex chamber. Figure 2.17 shows the collision of flows from the large and small flow pipes and the resultant conflux in the vortex chamber. In other words, the tangential components of the momenta from the large and small flow pipes must have the same magnitude and opposite directions to each other, or

$$Q_S V_S \sin \varphi - Q_L V_L \sin(\varphi + \phi) = 0, \quad (2.1)$$

where Q is flow rate, V velocity, and ϕ and φ the angles defined in Fig. 2.17. The suffixes, S and L, indicate quantities for small and large flows respectively.

In addition to that, the sum of the radial components of the momenta from the large and small flow pipes must have the same magnitude as the momentum of the conflux and the same direction, or

$$-Q_S V_S \cos \varphi - Q_L V_L \cos(\varphi + \phi) = (Q_S + Q_L) V_O, \quad (2.2)$$

where V_O (<0) is the inward velocity of the resultant conflux.

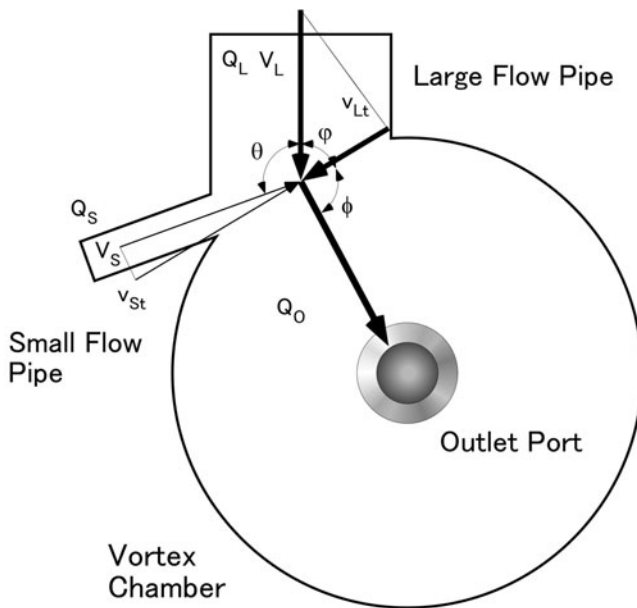


Fig. 2.17 Collision of large and small flows in the vortex chamber for large flow injection is considered. The angle is so designed that the angular momentum becomes zero. Additionally, radial momentum balance is also taken into account for stable formation of the resultant flow

If (2.2) is satisfied, there will be no pressure gradient at the collision point of the large and small flows so that the conflux can be stable. The collision angle, $\theta = \pi - \phi$, and the dimensions of the large and small flow pipes are selected to satisfy the condition mentioned above. The resultant conflux then goes straight to the outlet port of the vortex chamber without forming any vortex there.

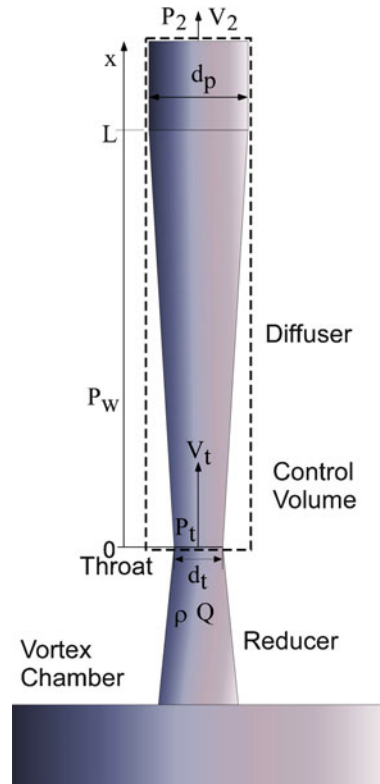
The flow then enters the outlet nozzle. Given that the reducer produces a small energy loss, the flow rate is mainly controlled by the throat for large flow injection. Figure 2.18 shows the outlet nozzle and the control volume to examine the momentum balance of the flow in the diffuser. Applying the momentum balance to the control volume, the pressure of the throat, P_t , is determined by the following equation of the momentum balance;

$$P_t \frac{\pi}{4} d_p^2 + \bar{C}_p \frac{1}{2} \rho V_t^2 \frac{\pi}{4} (d_p^2 - d_t^2) + \rho Q V_t = P_2 \frac{\pi}{4} d_p^2 + \rho Q V_2, \quad (2.3)$$

where P is pressure, d diameter, V velocity, Q flow rate, and ρ the density of fluid. The suffixes, t, 2, p and w, indicate the quantities at the throat, the outlet section of the control volume, the outlet pipe and the diffuser wall, respectively. The mean pressure coefficient is the mean value of the pressure coefficient over the diffuser wall, and given by

Fig. 2.18 The pressure at the throat is determined by the momentum balance of the flow in the diffuser.

The dotted line rectangle is the control volume for which the momentum balance is considered



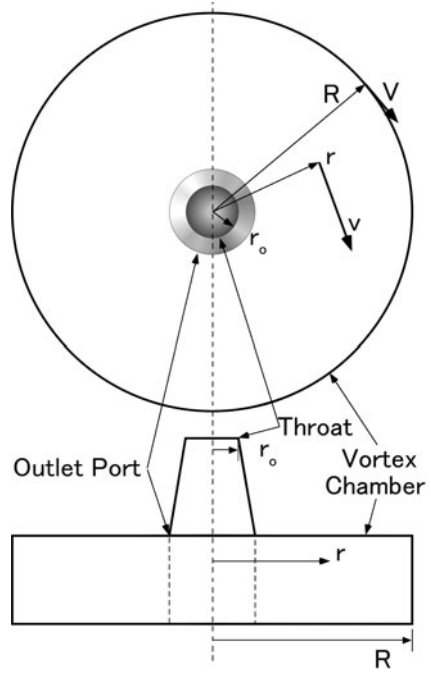
$$\bar{C}_p \equiv \frac{2}{L(d_2 + d_t)} \int_0^L \frac{P_w - P_t}{\rho V_t^2/2} \left(d_t + \frac{d_2 - d_t}{L} x \right) dx. \quad (2.4)$$

The first term on the left-hand side of (2.3) is the force acting on the upstream cross section of the control volume, the second term is the force acting on the wall of the diffuser, and the third term is the momentum flowing in the control volume. The first term on the right-hand side of (2.3) is the force acting on the downstream cross-section of the control volume and the second term is the momentum flowing out of the control volume. If cavitation occurs at the throat, pressure on the diffuser wall may vary and affect the flow rate of the damper.

For small flow injection, the small flow pipe is tangentially attached to the vortex chamber in order to make a strong vortex in the vortex chamber. Figure 2.19 shows the one-dimensional model of a vortex for small flow injection. The tangential velocity, v , at radius, r , is expressed as;

$$v = V \left(\frac{r}{R} \right)^n, \quad (2.5)$$

Fig. 2.19 A one-dimensional model of a vortex with respect to radius, r , is considered in the vortex chamber for small flow injection



where R is the radius of the vortex chamber, and V the velocity at $r = R$. If $n = 1$, (2.5) expresses a forced vortex, while if $n = -1$, (2.5) expresses a free vortex. Practically, n is between -1 and 1 , and depends on the configuration and the size of the vortex chamber and the property of water.

Figure 2.20 shows the distributions of the dimensionless tangential velocity, v/V , with respect to the dimensionless radius, r/R , and with the parameter of the exponent, n , using (2.5). If a free vortex can be formed in the vortex chamber, a large tangential velocity will be formed near the center of the vortex for $n < 0$. A free vortex for $n = -1$ conserves its angular momentum for all values of the radius. Therefore, less energy loss will conserve a large amount of its angular momentum and make a strong vortex in the vortex chamber.

The equation of motion yields the pressure drop, Δp , from the radius, R , to an arbitrary radius, r , using (2.5) as:

$$\Delta p = \frac{1}{n} \frac{\rho}{2} V^2 \left\{ 1 - \left(\frac{R}{r} \right)^{2n} \right\}. \quad (2.6)$$

From (2.6), the pressure drop coefficient from the radius, R , to the radius of the throat, r_o , is defined as

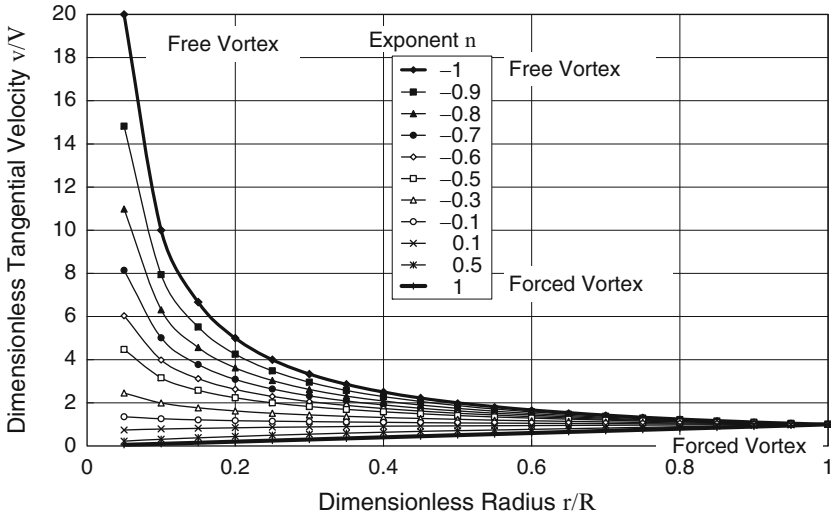


Fig. 2.20 This chart shows the distributions of the dimensionless tangential velocity, v/V , with respect to the dimensionless radius, r/R , for the parameter of the exponent, n , from the one-dimensional model of (2.5)

$$\zeta_s \equiv -\frac{\Delta p}{\rho V^2/2} = \frac{1}{n} \left\{ \left(\frac{R}{r_o} \right)^{2n} - 1 \right\}. \quad (2.7)$$

Figure 2.21 shows the pressure drop coefficient with respect to the vortex radius ratio. The larger the vortex radius ratio is, the larger the pressure drop coefficient of the vortex damper is. Moreover a free vortex, or $n = -1$, yields the largest pressure drop among the exponents $n = -1$ to 1. For a larger vortex radius ratio, a throat is inserted in the outlet nozzle. Furthermore, a diffuser is used to connect the throat to the outlet pipe to recover static pressure for large flow injection. The outlet pipe has the same diameter as that of the injection pipe and connects the outlet nozzle to the injection pipe.

The structure of a vortex in the vortex chamber is more complicated than that of the one-dimensional model. Velocity boundary layers practically develop on the upper- and lower-disk walls of the vortex chamber, while an inviscid swirl flow develops between them. Since viscosity reduces tangential velocity, the centrifugal force is so weak that the radial component of velocity becomes larger in the boundary layers than that in the inviscid vortex. This is the reason why the exponent, n , varies between -1 and 1. The swirl flow actually accelerates its tangential velocity component as it goes inward within the chamber. The accelerating flow and high Reynolds number generally restrain and suppress the development of the thickness of the boundary layers. Consequently, if the height of the vortex chamber is sufficiently larger than the thicknesses of the boundary layers, viscosity will negligibly affect the flow to yield a strong vortex in the chamber.

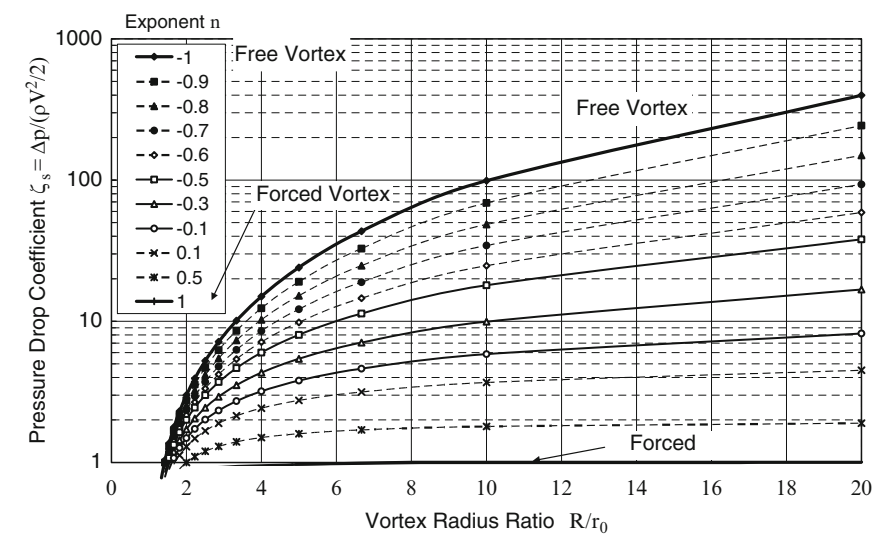


Fig. 2.21 Pressure drop coefficient, Δp , is shown here with respect to vortex radius ratio, R/r_0 . The larger the vortex radius ratio is, the larger the pressure drop coefficient of the vortex damper is. The free vortex yields the largest pressure drop

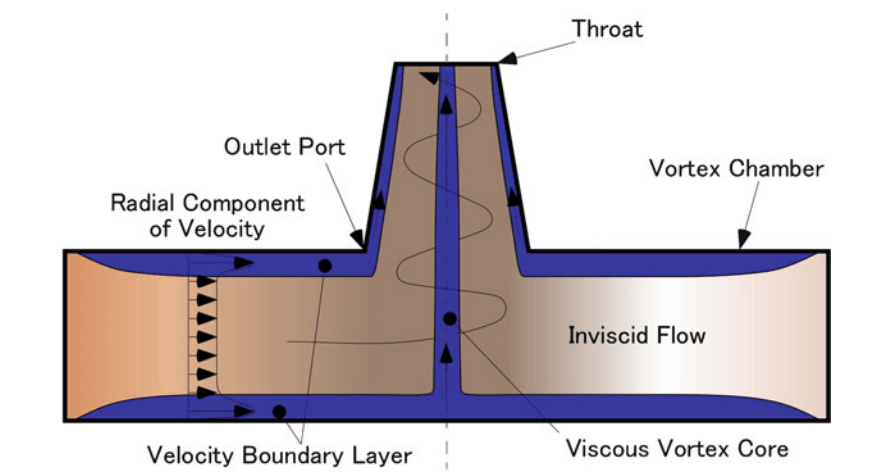


Fig. 2.22 This is the estimated structure of the vortex in the vortex chamber. There will be viscous boundary layers on the upper- and lower-disk walls. There will be a viscous vortex core at the center of the chamber. If the viscous boundary layers strongly affect the flow, velocity of the inviscid flow may be reduced

The estimated structure of the vortex in the chamber is shown in Fig. 2.22. A viscous vortex core will be formed at the center of the vortex. The flow in the boundary layer on the lower-disk wall will go into the viscous core, while the flow

in the boundary layer on the upper-disk wall will go along the wall of the reducer to the throat. Inviscid flow will form a swirl flow between them.

If influence of viscosity in the boundary layers is not negligible, flow patterns in the chamber will be more complicated. High swirls with small rate of total flow may cause a reverse flow in the inviscid vortex and form a so-called doughnut pattern near the outlet port. This pattern may appear when the flow rate in the boundary layers due to large pressure drop induced by high swirls is larger than the supplied flow rate into the chamber.

Even if an ideal inviscid swirl with negligible boundary layers is formed in the vortex chamber, the vortex core cannot be neglected. In order to examine this influence of viscosity, a combined model of a nonstretched vortex with a stretched vortex is examined as shown in Fig. 2.23 [11]. The cylindrical coordinates are adopted. The radii of the vortex chamber and the outlet port are r_1 and r_0 , respectively. The height of the vortex chamber is H . The tangential and radial components of velocity are v_θ and v_r , respectively. r is radius and p is pressure. Suffices 0 and 1 indicate quantities at r_0 and r_1 , respectively.

The following assumptions are used.

1. The flow is axisymmetric and depends only on radius, r .
2. The flow is laminar incompressible steady viscous flow.
3. The flow is a stretched vortex in the central region with $r < r_0$, and a non-stretched vortex in all other regions with $r_0 < r < r_1$.

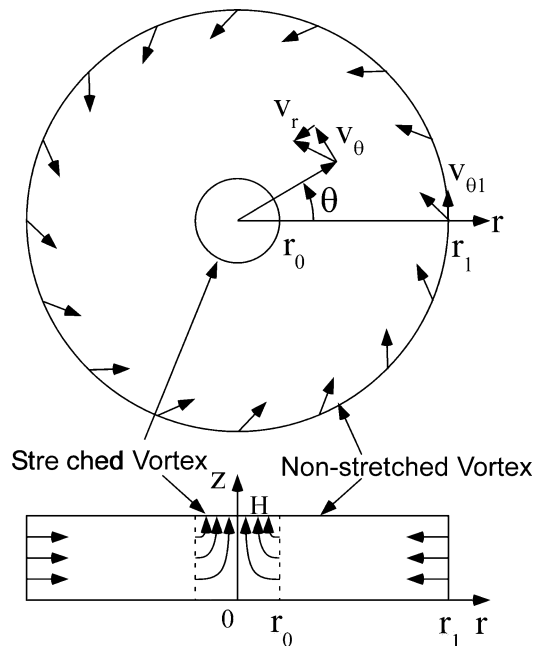


Fig. 2.23 A combined model of a nonstretched vortex with a stretched vortex is examined here. The flow is a stretched vortex for $r < r_0$, and a nonstretched vortex for $r_0 < r < r_1$. The boundary layers on the upper- and lower-disk walls are assumed to be negligible and small

4. The velocity and velocity gradient at the boundary of these regions at $r = r_0$ are continuous of their own.

The boundary conditions are $v_r = v_\theta = 0$ for $r = 0$, $v_\theta = v_{\theta 0}$, $p = p_0$ for $r = r_0$, and $v_\theta = v_{\theta 1}$ for $r = r_1$.

We let the flow rate be Q . The equation of continuity gives the characteristic flow rate, q as

$$q \equiv \frac{Q}{2\pi H} = -rv_r; \text{ for } r_0 \leq r \leq r_1, \quad (2.8)$$

and the gradient of velocity component in the z -direction as

$$\frac{\partial v_z}{\partial z} = -\frac{1}{r} \frac{\partial}{\partial r}(rv_r) \equiv \frac{2q}{r_0^2} = \text{const}; \text{ for } r \leq r_0 \quad (2.9)$$

Equation (2.9) represents a stretched vortex, while (2.8) is a nonstretched vortex. The r -component of the velocity is given by these equations for nonstretched and stretched vortices.

The equation of motion yields

$$\rho \left(v_r \frac{\partial v_r}{\partial r} - \frac{v_\theta}{r} + v_z \frac{\partial v_r}{\partial z} \right) = -\frac{\partial p}{\partial r}, \quad (2.10)$$

and

$$v_r \frac{1}{r} \frac{\partial}{\partial r}(rv_\theta) = v \frac{\partial}{\partial r} \left[\frac{1}{r} \frac{\partial}{\partial r}(rv_\theta) \right]. \quad (2.11)$$

Equation (2.11) has no pressure term and can be solved under boundary conditions to give the distributions of the θ -component of the velocity in the vortex chamber. Equation (2.10) then gives the pressure distributions using the velocity distributions in it.

We define the dimensionless parameters as:

$$r^* \equiv \frac{r}{r_0}, \quad r_1^* \equiv \frac{r_1}{r_0}, \quad q^* \equiv \frac{q}{v}, \quad v_\theta^* \equiv \frac{v_\theta}{v_{\theta 1}}, \quad p^* \equiv \frac{p - p_0}{\rho v_{\theta 1}^2}, \quad \text{and} \quad v_{\theta 0}^* \equiv \frac{v_{\theta 0}}{v_{\theta 1}}.$$

The dimensionless flow rate, q^* , is a kind of Reynolds number, and the dimensionless pressure, p^* , is a kind of Euler number. $v_{\theta 0}^*$ is the inner boundary condition which smoothly connects the velocity distributions of the stretched and nonstretched vortices.

Equation (2.11) gives the solution of the tangential velocity component as follows:

If $q^* \neq 0, 2$,

$$v_{\theta}^* = \frac{r_1^*}{r^*} \frac{2 - q^* - (2 - q^* r_1^{*2-q^*}) \exp(-q^*/2)}{2 - q^* - (2 - q^* r_1^{*2-q^*}) \exp(-q^*/2)} \text{ for } 1 \leq r^* \leq r_1^*, \quad (2.12a)$$

$$v_{\theta}^* = \frac{r_1^*}{r^*} \frac{(2 - q^*) [1 - \exp(-q^* r_1^{*2}/2)]}{2 - q^* - (2 - q^* r_1^{*2-q^*}) \exp(-q^*/2)}; \text{ for } r^* \leq 1. \quad (2.12b)$$

If $q^* = 2$,

$$v_{\theta}^* = \frac{r_1^*}{r^*} \frac{1 - (1 - 2 \ln r^*) \exp(-1)}{1 - (1 - 2 \ln r_1^*) \exp(-1)}; \text{ for } 1 \leq r^* \leq r_1^*, \quad (2.13a)$$

$$v_{\theta}^* = \frac{r_1^*}{r^*} \frac{1 - \exp(-r^{*2})}{1 - (1 - 2 \ln r_1^*) \exp(-1)}; \text{ for } r^* \leq 1. \quad (2.13b)$$

And, if $q^* = 0$,

$$v_{\theta}^* = \frac{r^*}{r_1^*}; \text{ for } 0 \leq r^* \leq r_1^*. \quad (2.14)$$

These equations are continuous to each other both for $q^* = 2$ and 0. Furthermore, these equations show that the dimensionless physical number used to determine the tangential velocity, v_{θ} , is only the Reynolds number, q^* . A forced vortex is given by (2.14) for $q^* = 0$, and a free vortex, by (2.12) for $q^* \rightarrow \infty$. In other words, a forced vortex is given only for a vortex with zero flow rate, and a free vortex is given only for inviscid flow. These solutions are more complicated than the one-dimensional vortex given by (2.5), but do not need to assume the exponent, n .

Some example solutions of these equations are shown in Fig. 2.24. The calculation conditions are $r_1^* = 1$ for the stretched vortices, and $r_1^* = 10$ for the combined vortices. The graphs compare the tangential velocity distributions of stretched vortices, or $r_0/r_1 = 1$, and combined vortices with the ratio of the radii, $r_0/r_1 = 0.1$. The tangential velocity in the region of $r^* = 0.1$ – 1.0 comes close to the free vortex when $q^* = 500$ for the stretched vortex, and $q^* = 7$ for the combined vortex. Thus, the nonstretched vortex has an advantage to make a strong vortex. That is because a stretched vortex loses its angular momentum rapidly, while a nonstretched vortex conserves its angular momentum better than a stretched vortex does. It is seen that the maximum tangential velocity of the combined vortex is formed in the stretched vortex. It implies that a nonstretched vortex preserves its angular momentum well and forms the maximum tangential velocity at the innermost location so that the stretched vortex can make the maximum tangential velocity inside itself.

Hereafter, the equations representing pressure distributions are examined. The inner boundary condition, $v_{\theta 0}^*$, is given for $r^* = 1$ by (2.12), (2.13) and (2.14).

Equation (2.10) gives the solution of the pressure as follows:

If $q^* \neq 0, 1, 2$

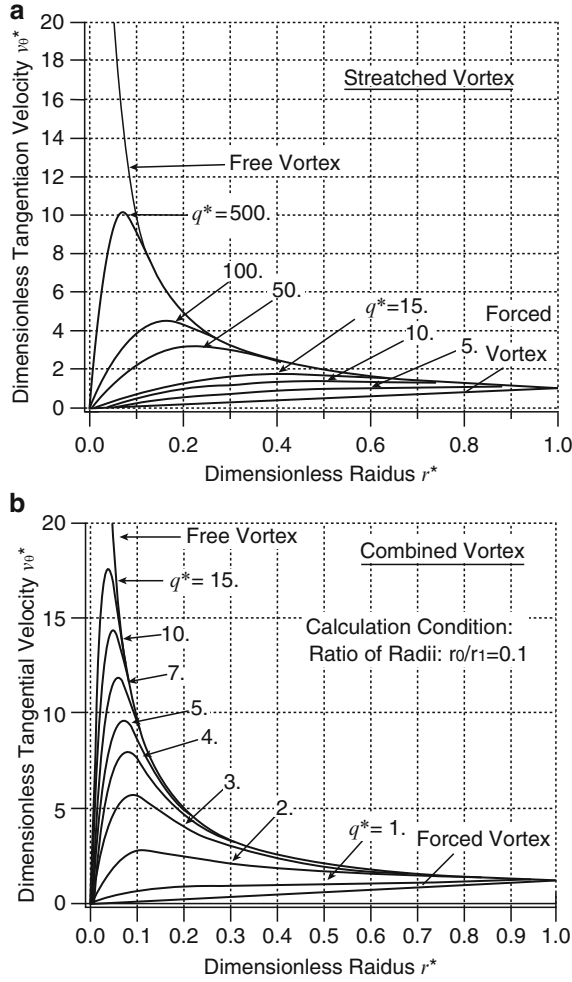


Fig. 2.24 Tangential velocity distributions of stretched and combined vortices. The stretched vortex yields a tangential velocity distribution close to that of a free vortex at the dimensionless flow rate of $q^* = 500$, while the combined vortex yields a tangential velocity distribution collapsed on that of a free vortex at the dimensionless flow rate of $q^* = 15$

$$\begin{aligned}
 p^* = & \frac{(r_1^* - v_{\theta 0}^*)^2 (r_1^{*2-q^*} - 1)}{2(1 - q^*)(r_1^{*2-q^*} - 1)^2} - \frac{2(r_1^* - v_{\theta 0}^*)}{\frac{q}{v}(r_1^{*2-q^*} - 1)} \left(v_{\theta 0}^* - \frac{r_1^* - v_{\theta 0}^*}{r_1^{*2-q^*} - 1} \right) \\
 & \times \left(r_1^{*-q^*} - 1 \right) - \frac{1}{2} \left[\left(v_{\theta 0}^* - \frac{r_1^* - v_{\theta 0}^*}{r_1^{*2-q^*} - 1} \right)^2 + \left(\frac{q}{r_0 v_{\theta 1}} \right)^2 \right] \\
 & \times \left(\frac{1}{r_1^{*2}} - 1 \right); \text{ for } 1 \leq r^* \leq r_1^*, \quad (2.15a)
 \end{aligned}$$

$$\begin{aligned}
p^* = & \frac{(2 - q^*)^2 r_1^{*2} q^* \sum_{n=1}^{\infty} \frac{1}{nn!} \left(-\frac{q^*}{2}\right)^n (1 - 2^n)(r^{*2n} - 1)}{2[2 - q^* + (q^* r_1^{*2-q^*} - 2) \exp(-q^*/2)]^2} \\
& - \frac{(2 - q^*)^2 r_1^{*2} \left\{ \frac{1}{r^{*2}} \left[\exp\left(-\frac{q^* r^{*2}}{2}\right) - 1 \right]^2 - \left[\exp\left(-\frac{pq^*}{2}\right) - 1 \right]^2 \right\}}{2[2 - q^* + (q^* r_1^{*2-q^*} - 2) \exp(-q^*/2)]^2} \\
& - \frac{1}{2} \left(\frac{q}{v_{\theta 1} r_0} \right)^2 \left[\frac{1}{r^{*2}} - 1 + \left(\frac{2H}{r_0} \right)^2 \left(1 - \frac{z}{H} \right)^2 \right] - \frac{g}{v_{\theta 1}^2} \\
& \times (z - H); \text{ for } 0 < r^* \leq 1,
\end{aligned} \tag{2.15b}$$

$$\begin{aligned}
p^* = & \frac{(2 - q^*)^2 r_1^{*2} \left\{ q^* \sum_{n=1}^{\infty} \frac{1}{nn!} \left(-\frac{q^*}{2}\right)^n (2^n - 1) + \left[\exp\left(-\frac{q^*}{2}\right) - 1 \right]^2 \right\}}{2[2 - q^* + (q^* r_1^{*2-q^*} - 2) \exp(-q^*/2)]^2} \\
& - \frac{1}{2} \left(\frac{q}{v_{\theta 1} r_0} \right)^2 \left[-1 + \left(\frac{2H}{r_0} \right)^2 \left(1 - \frac{z}{H} \right)^2 \right] - \frac{g}{v_{\theta 1}^2} (z - H);
\end{aligned} \tag{2.15c}$$

for $r^* = 0$.

If $q^* = 2$,

$$\begin{aligned}
p^* = & \frac{(r_1^* - v_{\theta 0}^*)^2}{4 \ln r_1^*} \left[\frac{1}{r^{*2}} (2 \ln^2 r^* + 2 \ln r^* + 1) - 1 \right] - \frac{r_1^* - v_{\theta 0}^*}{2 \ln r_1^*} \\
& \times \left[\frac{1}{r^{*2}} (2 \ln r^* + 1) - 1 \right] - \frac{1}{2} \left\{ v_{\theta 0}^{*2} + \left(\frac{q}{r_0 v_{\theta 1}} \right)^2 \right\} \\
& \times \left(\frac{1}{r^{*2}} - 1 \right); \text{ for } 1 \leq r^* \leq r_1^*,
\end{aligned} \tag{2.16a}$$

$$\begin{aligned}
p^* = & \frac{2r_1^{*2} \sum_{n=1}^{\infty} \frac{1}{nn!} (-1)^n (1 - 2^n) [r^{*2n} - 1]}{2[1 + (2 \ln r_1^* - 1) \exp(-1)]^2} \\
& - \frac{r_1^{*2} \left\{ \frac{1}{r^{*2}} [\exp(-r^{*2}) - 1]^2 - [\exp(-1) - 1]^2 \right\}}{2[1 + (2 \ln r_1^* - 1) \exp(-1)]^2} \\
& - \frac{1}{2} \left(\frac{q}{v_{\theta 1} r_0} \right)^2 \left[\frac{1}{r^{*2}} - 1 + \left(\frac{2H}{r_0} \right)^2 \left(1 - \frac{z}{H} \right)^2 \right] - \frac{g}{v_{\theta 1}^2} \\
& \times (z - H); \text{ for } 0 < r^* \leq 1,
\end{aligned} \tag{2.16b}$$

$$\begin{aligned}
p^* &= \frac{r_1^{*2} \left\{ 2 \sum_{n=1}^{\infty} \frac{1}{nn!} (-1)^n (2^n - 1) + [\exp(-1) - 1]^2 \right\}}{2[1 + (2 \ln r_1^* - 1) \exp(-1)]^2} \\
&\quad - \frac{1}{2} \left(\frac{q}{v_{\theta 1} r_0} \right)^2 \left[-1 + \left(\frac{2H}{r_0} \right)^2 \left(1 - \frac{z}{H} \right)^2 \right] - \frac{g}{v_{\theta 1}^2} (z - H); \text{ for } r^* \\
&= 0.
\end{aligned} \tag{2.16c}$$

If $q^* = 1$,

$$\begin{aligned}
p^* &= \frac{(r_1^* - v_{\theta 0}^*)^2}{(r_1^* - 1)^2} \ln r^* - \frac{2(r_1^* - v_{\theta 0}^*)}{r_1^* - 1} \left(\frac{v_{\theta 0}}{v_{\theta 1}} - \frac{r_1^* - v_{\theta 0}^*}{r_1^* - 1} \right) (r^* - 1) - \frac{1}{2} \\
&\quad \times \left[\left(v_{\theta 0}^* - \frac{r_1^* - v_{\theta 0}^*}{r_1^* - 1} \right)^2 + \left(\frac{q}{r_0 v_{\theta 1}} \right)^2 \right] \left(\frac{1}{r^{*2}} - 1 \right); \text{ for } 1 \leq r^* \leq r_1^*, \\
\end{aligned} \tag{2.17a}$$

$$\begin{aligned}
p^* &= \frac{r_1^{*2} \sum_{n=1}^{\infty} \frac{1}{nn!} \left(-\frac{1}{2} \right)^n (1 - 2^n) (r^{*2n} - 1)}{2[1 + (r_1^{*2-q^*} - 2) \exp(-1/2)]^2} \\
&\quad - \frac{r_1^{*2} \left\{ \frac{1}{r^{*2}} \left[\exp\left(-\frac{r^{*2}}{2}\right) - 1 \right]^2 - \left[\exp\left(-\frac{1}{2}\right) - 1 \right]^2 \right\}}{2[1 + (r_1^{*2-q^*} - 2) \exp(-1/2)]^2} \\
&\quad - \frac{1}{2} \left(\frac{q}{v_{\theta 1} r_0} \right)^2 \left[\frac{1}{r^{*2}} - 1 + \left(\frac{2H}{r_0} \right)^2 \left(1 - \frac{z}{H} \right)^2 \right] - \frac{g}{v_{\theta 1}^2} \\
&\quad \times (z - H); \text{ for } 0 < r^* \leq 1,
\end{aligned} \tag{2.17b}$$

$$\begin{aligned}
p^* &= \frac{r_1^{*2} \left\{ q^* \sum_{n=1}^{\infty} \frac{1}{nn!} \left(-\frac{1}{2} \right)^n (2^n - 1) + \left[\exp\left(-\frac{1}{2}\right) - 1 \right]^2 \right\}}{2[1 + (r_1^* - 2) \exp(-1/2)]^2}; \text{ for } r^* = 0. \\
&\quad - \frac{1}{2} \left(\frac{q}{v_{\theta 1} r_0} \right)^2 \left[-1 + \left(\frac{2H}{r_0} \right)^2 \left(1 - \frac{z}{H} \right)^2 \right] - \frac{g}{v_{\theta 1}^2} (z - H)
\end{aligned} \tag{2.17c}$$

If $q^* = 0$,

$$p^* = \frac{(r_1^* - v_{\theta 0}^*)^2 (r^{*2} - 1)}{2(r_1^{*2} - 1)^2} - \frac{2(r_1^* - v_{\theta 0}^*)}{r_1^{*2} - 1} \left(v_{\theta 0}^* - \frac{r_1^* - v_{\theta 0}^*}{r_1^{*2} - 1} \right) \ln r^* - \frac{1}{2} \left(v_{\theta 0}^* - \frac{r_1^* - v_{\theta 0}^*}{r_1^{*2} - 1} \right)^2 \left(\frac{1}{r^{*2}} - 1 \right); \text{ for } 1 \leq r^* \leq r_1^*, \quad (2.18a)$$

$$p^* = \frac{1}{2} r_1^{*2} [r^{*2} - 1] - \frac{g}{v_{\theta 1}^2} (z - H); \text{ for } 0 \leq r^* \leq 1. \quad (2.18b)$$

These equations are continuous to each other for $q^* = 2, 1$ and 0 . The pressure drop is a function of not only a Reynolds number but also the radial inlet velocity, v_{r1} , and the gravity. Fig. 2.25 shows some pressure distributions of stretched and combined vortices for $q^* = 1$ to 15 . The calculation conditions are $r_1^* = 1$ for the stretched vortices, and $r_1^* = 10$ for the combined vortices the same as for the tangential velocities in Fig. 2.24. The inlet radial velocity is given as $v_{r1}/v_{\theta 1} = 1$ for both vortices and $z = 0$ in common. The pressure drop of the combined vortex for $q^* = 15$ is about 100 times that of the stretched vortex for $q^* = 15$. This is the reason why we need to select the form of the vortex chamber.

2.5.5 Transition of Water Level in the Standpipe

The important role of the standpipe is to prevent gas leakage at the changeover of flow rate and during the small flow injection in addition to detection of water level in the accumulator tank. The size of the standpipe is determined by the prevention of gas leakage at the changeover.

The behavior of the water level during the flow changeover is shown in Fig. 2.26. There are three steps after the formation of the water level in the standpipe as follows:

Step 0: Water in the standpipe is still flowing at the end of large flow injection.

Then, the water level in the accumulator tank drops across the inlet port of the standpipe, and water stops flowing in. This forms a water level in the standpipe.

Step 1: The water level still descends due to the inertia of the water column in the standpipe. The water level then has to stop to form a stationary water level so that gas leakage is prevented. The static pressure at the exit of the large flow pipe is smaller than the pressure in the accumulator tank at the amount of the dynamic pressure in the small flow pipe. The water level comes down once below the balanced level corresponding to the static pressure to stop its movement due to its inertia.

Step 2: Then, the static pressure at the exit of the standpipe pushes the water level back to the balanced level.

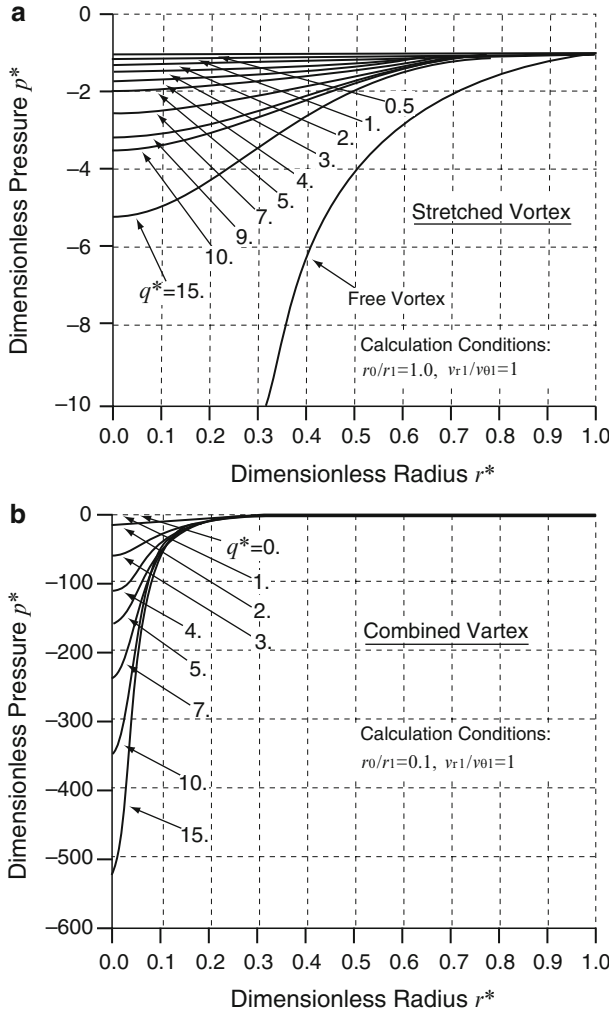


Fig. 2.25 Pressure distributions of stretched and combined vortices are shown for $q^* = 1$ to 15. A combined vortex yields much larger pressure drop than a stretched vortex does

Step 3: Thereafter, it stops at the balanced level and gradually drops along with the water level in the accumulator tank.

The schematic chart in Fig. 2.27 shows the behavior of the water level in the standpipe as time passes. For large flow injection, the inlet port of the standpipe is underwater. When the water level in the accumulator tank drops to the inlet port of the standpipe and the flow changeover is initiated, a water level in the standpipe appears and plummets due to the inertia of the water column and causes an undershoot. This undershoot produces a force to stop the movement of the water

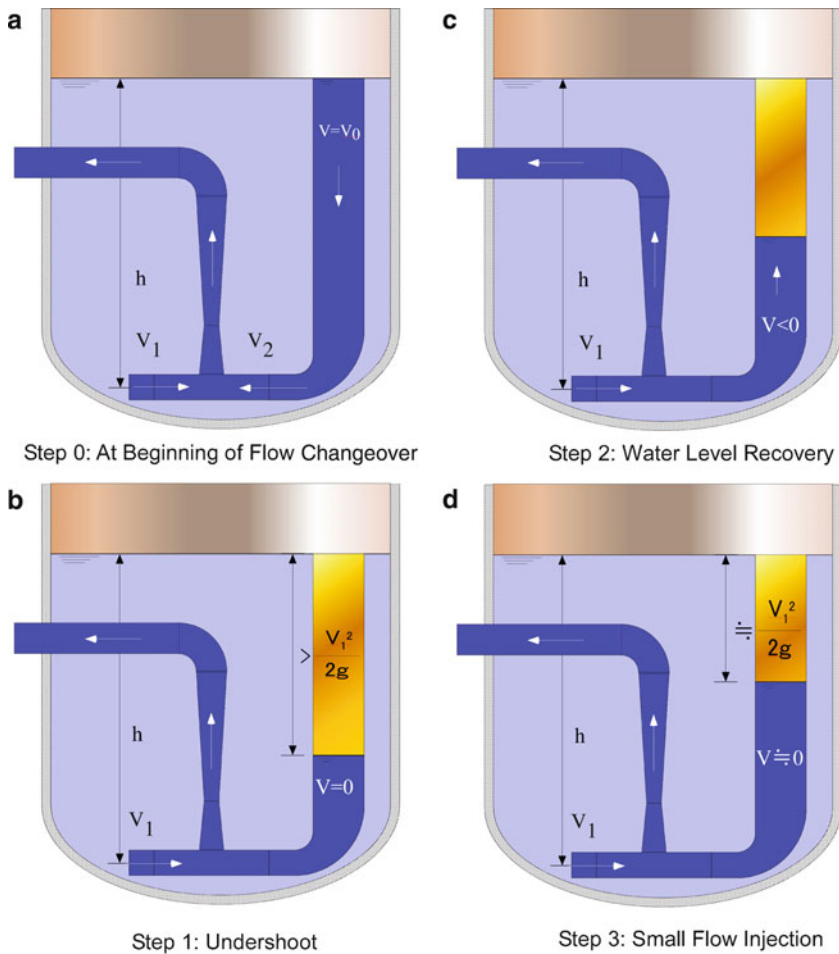


Fig. 2.26 At the flow changeover, the water level appears in the standpipe and undergoes the transition. The transition of water level is controlled by the momentum balance of the water column

column and recovers the water level to a balanced level with the static pressure at the exit of the standpipe which is equivalent to that of the large flow pipe. The water level then gradually decreases as the water level in the accumulator tank decreases for small flow injection.

The transition of the water column is controlled by the momentum balance. Figure 2.28 shows a one-dimensional model of the water column in the standpipe. The one-dimensional momentum equation applied to the water column is expressed as:

$$\frac{d}{dt}(hv) = -v^2 + gh - \zeta \frac{1}{2}|v|v - \left(gH - \frac{1}{2}v_s^2\right). \quad (2.19)$$

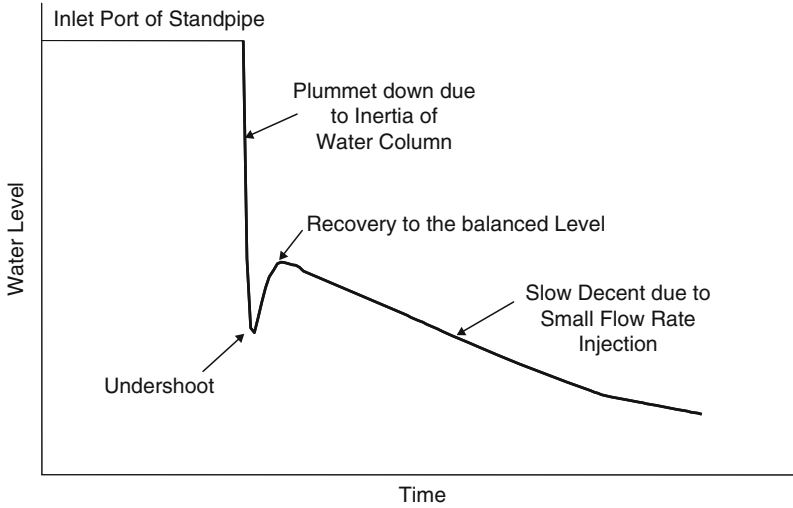
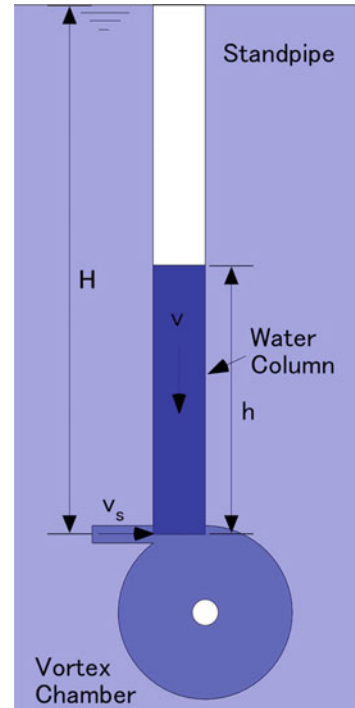


Fig. 2.27 Schematic chart showing transition of water level in the standpipe. When the water level in the accumulator tank falls below the inlet port of the standpipe, the water level also appears in the standpipe, and plummets due to its inertia to stop at the undershoot level. Then, it recovers to stop at the balanced level with the static pressure at the exit of the large flow pipe. The water level retains its balance with the static pressure at the exit of the large flow pipe during small flow injection

Fig. 2.28 The one-dimensional momentum model can explain the transition of the water column in the standpipe at the flow changeover. A control volume is applied to the water column to get the momentum balance to yield the one-dimensional momentum (2.19). The static pressure at the exit of the large flow pipe equals to the pressure in the accumulator tank minus dynamic pressure in the small flow



The notations are shown in Fig. 2.28 h and v are the length and the velocity of the water column, respectively. t is time and g is the gravitational acceleration. ζ is the loss coefficient of the standpipe. H is the water level in the accumulator tank. v_s is the velocity on the small flow pipe.

The term on the left-hand side of (2.19) is the momentum change rate of the water column. On the right-hand side: the first term is the outgoing momentum; the second term is the gravitational force; the third term is the resistance of the standpipe; and the fourth term is the static pressure at the exit of the standpipe. This equation is solved step by step with a small time interval to provide a maximum drop in the water level. The balanced level is given by (2.19) for $v = 0$ as:

$$h = H - \frac{1}{2g} v_s^2. \quad (2.20)$$

The comparison of the calculated maximum drops of water level in the standpipe by the one-dimensional momentum (2.19) to the measured values taken by the full-height 1/2-scale model is shown in Fig. 2.29 for the test conditions shown at Table 2.1. They are in good agreement with each other. The water levels are sustained in the standpipe, and they prevent gas leakage throughout, even for the severest Case 3. The initial velocity of the water column at the switchover is the main factor to determine the maximum drop of the water level in the standpipe. If the initial velocity is small, the maximum drop will be also small and preserve the water level in the standpipe to prevent gas leakage. Alternatively, if the initial velocity is too large, the maximum drop will so large that gas leakage may occur.

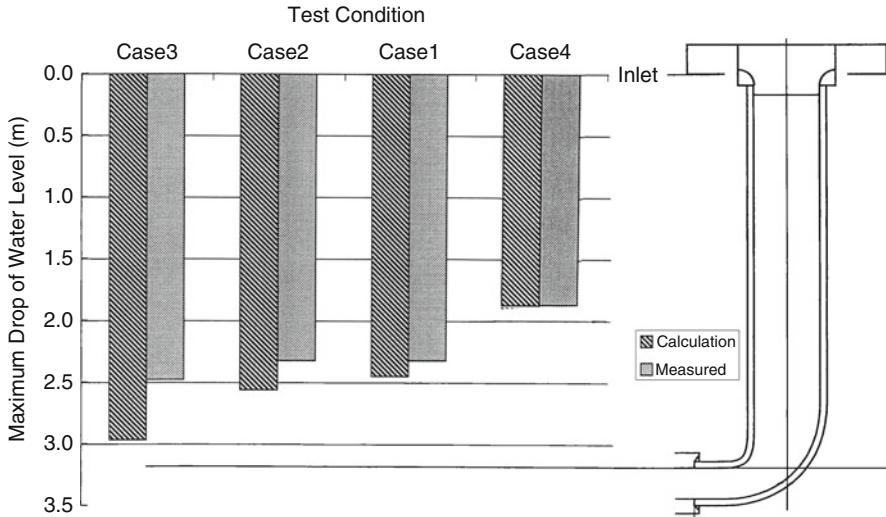


Fig. 2.29 The comparison of the calculated maximum drops of water level in the standpipe to the measured values shows good agreement between them

Table 2.1 Test conditions of injection under the actual pressure with the full-height 1/2-scale model apparatus at Takasago R&D Center, MHI

Test case	Pressure in test tank (MPaG)	Pressure in exhaust tank (MPaG)	Objective
Case 1	4.04	0.098	To obtain data for evaluation of ECCS performance during large LOCA
Case 2	4.53	0.098	To obtain data for high pressure design
Case 3	5.22	0.49	To obtain data of large differential pressure
Case 4	4.04	0.49	To obtain data of small differential pressure

Therefore, the cross-sectional area of the standpipe has to be determined by this calculation. The standpipe can be either a circular or square cylinder in shape. There should be a bell mouth at the inlet of the standpipe to rectify flow in it. The antivortex cap should give enough clearance on the inlet port of the standpipe so that it does not block the flow.

2.6 Confirmation Tests of the Advanced Accumulator

If a large break LOCA happens during operation of the Advanced Accumulator, the pressure in the accumulator tank decreases from about 4 MPa to about 1 MPa for large flow injection. Nitrogen gas could dissolve into the borated water kept in the accumulator tank on standby. Such dissolved nitrogen gas may form bubbles at low pressure locations and affect the flow rate characteristics of the Advanced Accumulator. Cavitation may also occur at the throat in the outlet nozzle of the flow damper due to high flow velocity. The required flow rate must be satisfied. At the end of large flow injection, the water level comes down close to the inlet port of the standpipe and may form a vortex and a water fall at the inlet port. The antivortex cap will prevent these free surface phenomena from forming to secure quick and reliable start of changeover of flow rate.

At flow changeover, the water level in the standpipe plummets to the minimal level and recovers to the balanced level. The minimal water level must be sustained in the standpipe to prevent gas leakage. The changeover of flow must be secure and quick to form a stable and strong vortex in the vortex chamber thereafter.

For small flow injection, the water level in the standpipe is lower than that in the accumulator tank according to the dynamic pressure in the small flow pipe. The required flow rate must be satisfied.

At the end of small flow injection, the Advanced Accumulator finishes its role and leaves water only in the dead-water region at the bottom of the accumulator tank.

The characteristics of the Advanced Accumulator are determined by the following factors:

- For large flow injection
 - Cavitation at the throat of the outlet nozzle may affect flow rates.
 - Cavitation factors and Reynolds numbers will be the key parameters to determine flow rates.
- For flow changeover
 - Flow injection is securely changed over at the determined level of water in the accumulator tank.
 - The transition of flow changeover is preferably finished in a short time.
- For small flow injection
 - A strong and steady vortex is formed in the vortex chamber.
 - A large pressure drop exists along the radius of the vortex chamber.

The confirmation tests were carried out to examine whether the expected performance was achieved by the operational principle of the Advanced Accumulator and to discuss the performance requirements. The confirmatory testing program was conducted as a joint study among the five Japanese utilities and MHI.

2.6.1 Purpose of Scale Testing

For the development of the Advanced Accumulator, the following items should be confirmed:

1. The principle of the flow damper
2. The performance of the flow damper during large and small flow injections
3. The influence of dissolved nitrogen gas on the performance of the flow damper
4. The dimensionless numbers (cavitation factor and flow coefficient) to represent flow characteristics
5. The independency of flow characteristics from scales of flow damper
6. The transition of water level in the standpipe at flow changeover
7. The water level in the accumulator tank at flow changeover with respect to the inlet port of the standpipe
8. The prevention of vortex formation by the antivortex cap at the end of large flow injection

Four kinds of scale models were made to confirm these items.

1. The 1/8.4-scale visualization tests were carried out to demonstrate the principle of switching flow to confirm Item 1.
2. The 1/3.5-scale visualization tests were carried out for demonstration of quick shutoff of flow into the standpipe to confirm Item 8.

3. The 1/5-scale visualization tests at low-pressure injections were carried out for acquisition of the flow rate characteristics of the flow damper to confirm Items 4 and 5.
4. The full-height 1/2-scale tests at the actual pressure injections were carried out to demonstrate the total characteristics of the actual Advanced Accumulator to confirm Items 2–7.

2.6.2 Principle of the Advanced Accumulator

The overall functions of the Advanced Accumulator were demonstrated by visualization tests of flow with the 1/8.4-scale model. The test apparatus consisted of an accumulator tank, a flow damper, an exhaust tank, and an injection pipe as shown in Fig. 2.30. The scale of the flow damper was 1/8.4, which was selected so that it could be moved anywhere for the tests. The vortex chamber was in an upright position. The front panel was made of transparent acrylic resin to observe water levels in the accumulator tank and the standpipe, and flow in the flow damper.

The objectives of the tests were:

1. Confirmation of the operational principle of the flow damper
2. Confirmation of behavior of water level in the standpipe at flow changeover and during small flow injection.

The test apparatus can visualize flows and water levels in the accumulator tank, the flow damper and the standpipe during large flow injection, changeover from large to small flow rates, and small flow injection. It can also be used to observe formation of a vortex in the vortex chamber. Finally, the motion of water level in the standpipe at flow changeover can be observed as well.

Since there was no special requirement for the test conditions, pressure in the Advanced Accumulator was set slightly lower than 0.1 MPaG, and the exhaust tank was opened to the atmosphere. A compressor supplied air to pressurize the tank in place of nitrogen gas. In addition to flow visualization, flow rate was measured and displayed on a screen. Pressure in the accumulator was monitored with a pressure gauge.

The basic performance of the accumulator was confirmed as follows.

1. When water level was higher than the top of the standpipe, or during large flow injection:
 - (a) Flows from the standpipe and the small flow pipe collided with each other, and the conflux directly went to the outlet port in the vortex chamber.
 - (b) A vortex was not formed in the vortex chamber.
 - (c) A large flow rate appeared.
 - (d) There was no gas-entraining vortex formed at the inlet port of the standpipe.

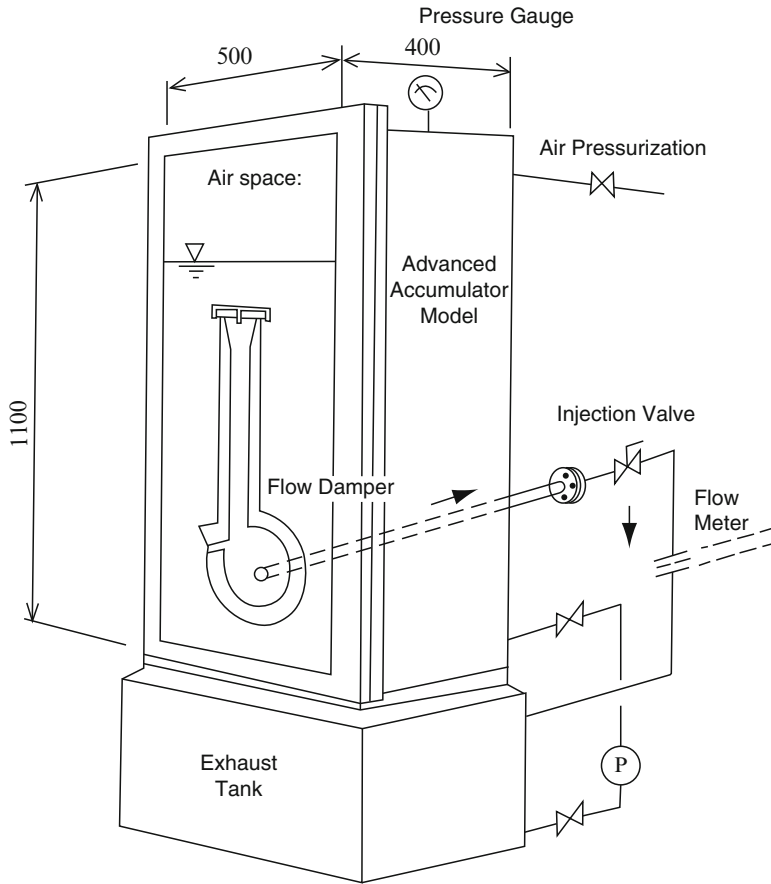


Fig. 2.30 1/8.4-scale model of the Advanced Accumulator used to demonstrate the principle. The flow damper was set at the upright position and the front wall was made of transparent acrylic resin to observe the water levels and the flow in it

2. During flow changeover:
 - (a) The water level that appeared in the standpipe plummeted to the minimal level and quickly recovered to the balanced level.
 - (b) The flow in the standpipe immediately stopped, and the water column was sustained in it.
 - (c) A vortex was quickly formed in the vortex chamber.
 - (d) Gas did not enter through the standpipe to the vortex chamber.
3. When water level was lower than the top of the standpipe, or during small flow injection:
 - (a) The flow from the standpipe stopped and only the flow from the small flow pipe came into the vortex chamber.

- (b) A strong and steady vortex was formed in the chamber.
- (c) A small flow rate appeared.

Thus, the principle of the Advanced Accumulator was successfully confirmed.

2.6.3 Confirmation of Quick Changeover

Quick changeover of flow and prevention of gas entrainment from the free surface of water were examined by visualization tests of the water surface with the 1/3.5-scale model. The test apparatus consisted of an antivortex cap, the upper part of the standpipe, and the middle part of the accumulator tank as shown in Fig. 2.31. There

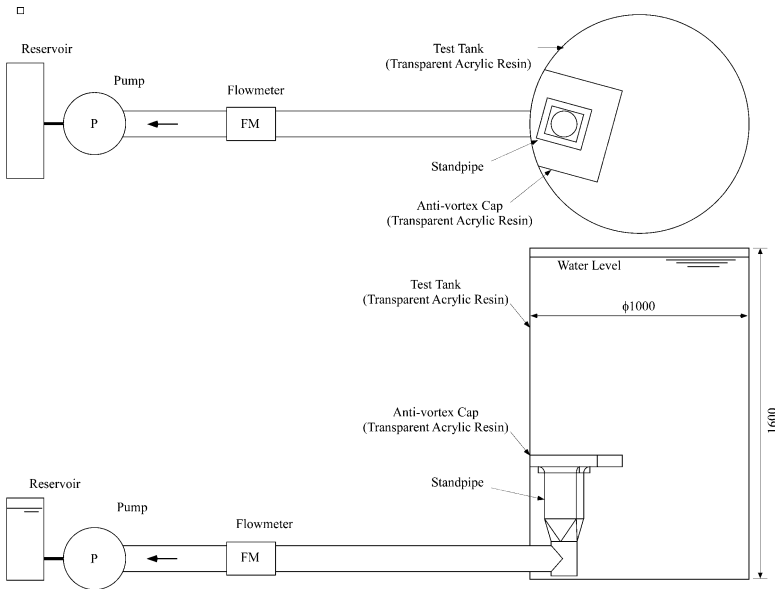


Fig. 2.31 1/3.5-scale model of the upper part of the standpipe and the anti-vortex cap in the accumulator tank used to confirm quick shutoff of flow into the standpipe

were also a pump and a flow meter in the pipe which are not shown in the figure. The accumulator tank and the antivortex cap were made of transparent acrylic resin to observe the shape and the behavior of water surfaces both in the tank and the antivortex cap. The scale of the model was 1/3.5, which was selected for easy observation of water surfaces.

The objectives of the tests were the certification of quick flow changeover and the prevention of vortex formation by the antivortex cap. The antivortex cap is known to prevent a vortex and a water fall causing gas entrainment at the inlet port of the standpipe. Without the antivortex cap, it was foreseen that gas entrainment due to a vortex and a water fall may affect the flow rate.

Because the tests were conducted to investigate the phenomena of water surfaces, a Froude number was adopted to determine the test conditions. The transition of flow rate at the tests was manually simulated as that of large flow injection of the Advanced Accumulator. Hence, the transition of the water level in the accumulator tank was simulated. The flow rate was measured by an ultrasonic flow meter in the injection pipe. The water level was measured by a ruler attached on the sidewall of the test tank. The transition and the phenomena of water levels were recorded on video.

Figure 2.32 shows examples of transitions of flow rate in the standpipe with and without the antivortex cap. In the case without the anti-vortex cap, gas entrainment started at 26 s. Fluctuation of the flow rate was generated for several seconds due to gas entrainment. It resulted from the formation of a vortex and a water fall at the inlet port of the standpipe. It took about 5 s for the flow rate to decrease to zero.

In the case with the antivortex cap, it took approximately 1 s for the flow rate to become zero after 25.5 s. There was no vortex or water fall formed on the inlet port of the standpipe. The flow rate thus switched more quickly than that without the antivortex cap.

Consequently, it was confirmed that the antivortex cap prevented formation of a vortex and a water fall causing gas entrainment, and it assured quick changeover of the flow rate.

2.6.4 Performance of the Flow Damper

Acquisition of the flow-rate characteristics of the flow damper was implemented by the low-pressure injection tests with the 1/5-scale model. The test facility consisted of a test tank, a flow damper model with a standpipe, an injection pipe and an exhaust tank as shown in Fig. 2.33. The configurations of the flow damper and the standpipe were similar to those of the actual accumulator for measurement of quantitative data of the flow damper. The flow damper was placed outside of the test tank. The lower-disk wall of the vortex chamber was made of transparent acrylic resin in order to observe and record flow in the vortex chamber on video. The 1/5-scale was selected so that several flow dampers could be installed and tested to acquire accurate data for evaluation of the characteristics of the flow damper. A resistance control valve was installed in the injection pipe to simulate the

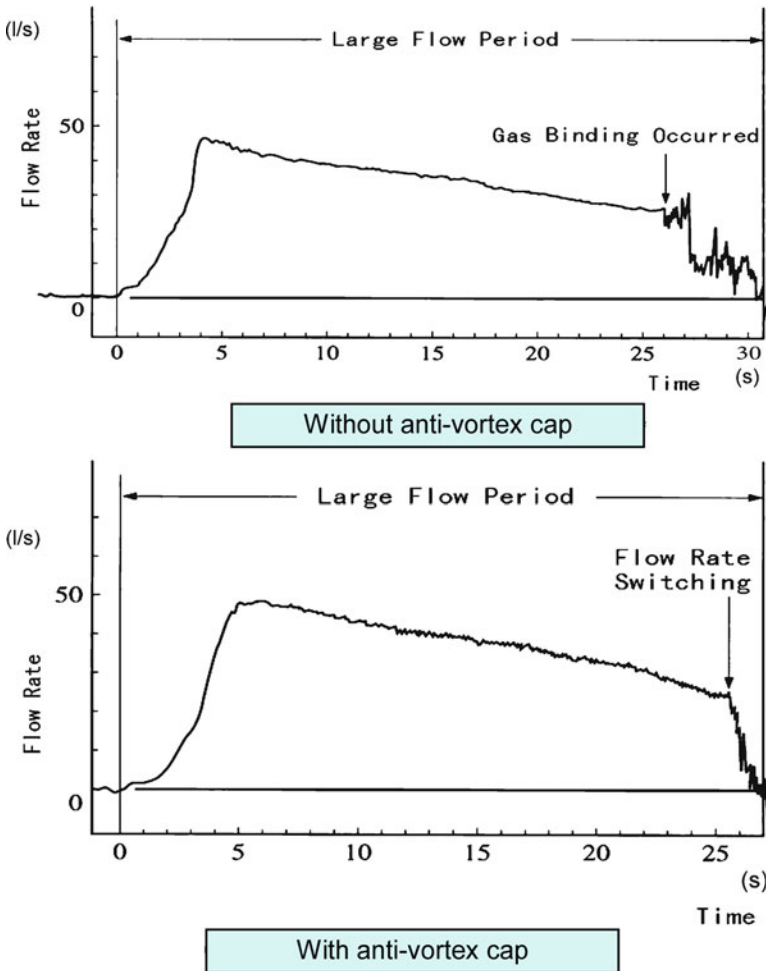


Fig. 2.32 Examples of flow rate transitions with and without the antivortex cap show that changeover of flow rate with the antivortex cap was much faster than that without the antivortex cap

flow resistance of the injection pipe of actual plants. There was an isolation valve at the end of the injection pipe. It was quickly opened to start injection of flow. The exhaust tank corresponded to the main coolant system. The test tank was supplied with and pressurized by nitrogen gas before every test.

The objectives of the tests were:

1. Confirmation of the operational principle of the flow damper
2. Acquisition of performance data during large and small flow injections

The dimensionless parameters of the flow damper are Reynolds number and cavitation factor. The flow rate of the flow damper is represented by the flow rate coefficient.

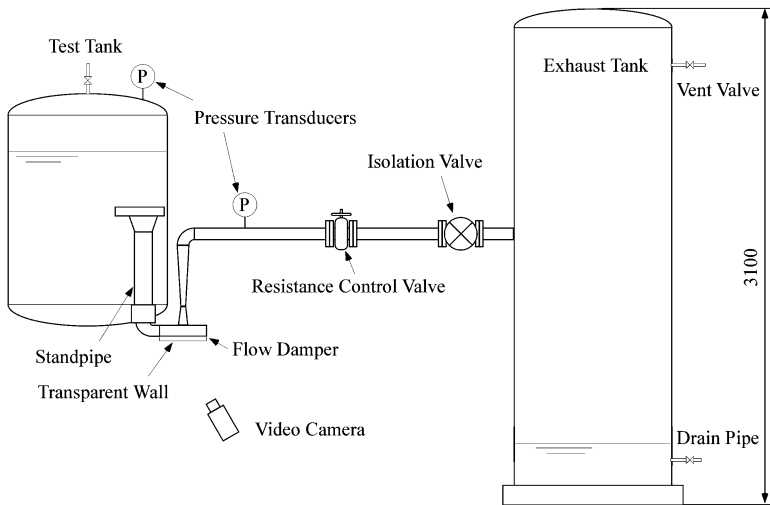


Fig. 2.33 1/5-scale test facility for acquisition of the characteristics of the flow damper. The flow damper was placed outside of the test tank for observation and recording of flow in the vortex chamber on video

If influence of viscosity on the characteristics of the flow damper is negligibly small, a Reynolds number can be excluded from consideration. This means that the characteristics of the flow damper taken by the 1/5-scale model collapse to those taken by the 1/2-scale model. The dependency on a Reynolds number is discussed later in this chapter. On the other hand, if cavitation occurs in the flow damper and affects the flow rate, the characteristics of the flow damper will depend on the cavitation factor. Consequently, the flow rate coefficient of the flow damper should be examined with respect to the cavitation factor. The test conditions were selected to get data in the widest range of cavitation factors possible in the test facility.

To derive the acquisition of flow rate characteristics, pressures in the test tank, the injection pipe, and the exhaust tank were measured with pressure transducers. Water levels in the test tank and the standpipe were measured by a differential pressure transducer and an electrocapacitance level meter, respectively. These data were recorded by a personal computer. The flow rates were calculated from the water level in the test tank. Moreover, flow rate coefficients and cavitation factors were calculated from these data.

The flow in the vortex chamber was observed through the transparent lower-disk wall and recorded on video to examine the vortex formation in it at changeover of flow rates. Figure 2.34 shows a set of flow images observed through the lower-disk wall of the vortex chamber. Ink was injected as a tracer from the small flow pipe on the bottom right side to indicate small flow, and from a small hole on the upper-disk wall to indicate large flow. The large flow pipe was located on the right top side of each photograph, and the outlet port was at the center.



Fig. 2.34 Visualized flows in the vortex chamber of the 1/5-scale model are shown. White lines are added as guides to indicate the observed flow directions. There was no vortex for the large flow injection, while a strong and steady vortex was formed for the small flow injection. The change-over of the flow from the large to small flow injections was quick and continuous

The left photograph for large flow injection shows both flows from the large and small flow pipes colliding with each other in the vortex chamber and the resultant confluent flow going straight to the outlet port. The central photograph for flow change-over shows transition of flow from the large to small flow injections, and how a vortex promptly began to form. The right photograph for small flow injection shows how flow from the small flow pipe tangentially entered in the vortex chamber and formed a strong and steady vortex in it.

Flow rate coefficient, C_v , and cavitation factor, σ_v , are defined as:

$$C_v = \frac{Q}{A_d \sqrt{2(p_a - p_{dT})/\rho}}, \quad (2.21)$$

and

$$\sigma_v = \frac{p_d - p_v}{p_a - p_{dT}}, \quad (2.22)$$

where Q is flow rate, A_d is the area of the injection pipe, p_a is pressure in the accumulator tank, p_d and p_{dT} are static and total pressures in the injection pipe, respectively. Finally, ρ and p_v are density and vapor pressure of fluid, respectively.

An example of the flow rate characteristics of the flow damper obtained by the 1/5-scale model is shown in Fig. 2.35. The data were divided into two groups for large and small flow injections. The flow rate coefficient depended on the cavitation factor for large flow injection, while it was independent of the cavitation factor for small flow injection. The data for cavitation factor near $\sigma_v = 9$ obtained at the last stage of small flow injection had relatively larger errors than the other data.

The ratio of the flow rate coefficient of the flow damper for large to small flow injection at cavitation factor, $\sigma_v = 4.5$, was about 10. It was confirmed that the flow damper could yield a large flow rate ratio. The flow rate characteristics were determined by the flow at the throat of the outlet nozzle for large flow injection. If cavitation occurred at the throat, the flow rate coefficient might be reduced.

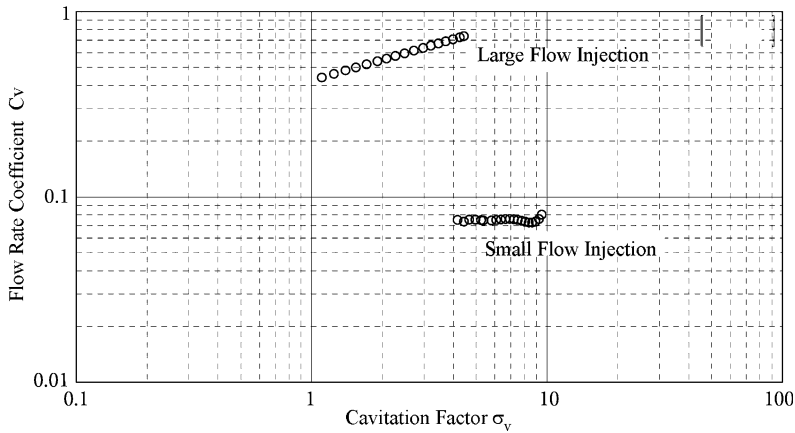


Fig. 2.35 Example flow rate characteristics of the flow damper obtained by the 1/5-scale model. The flow rate coefficients were clearly divided into two groups for large and small flow injections

The smaller the cavitation factor was, the bigger the reduction of the flow rate coefficient because of larger occurrence of cavitation.

For small flow injection, the flow rate characteristics were determined by a strong vortex in the vortex chamber. There was no cavitation at the throat of the outlet nozzle. This was why the flow rate coefficient was independent of the cavitation factor. There may be cavitation at the center of a strong vortex in the vortex chamber. But the reducer at the outlet port confined the cavitation within the vortex chamber so that it did not reach the throat.

2.6.5 Total Performance of the Advanced Accumulator

Acquisition of the data of the total performance was carried out with the full-height 1/2-scale model of the Advanced Accumulator under the actual pressure conditions. The test facility consisted of the accumulator model, which was the test tank of about 9 m in height, and contained the flow damper along with the standpipe, the injection pipe, and the exhaust tank as shown in Fig. 2.36. The auxiliary devices were composed of a liquid nitrogen tank and an evaporator to supply nitrogen gas to the accumulator tank and the exhaust tank. The exhaust tank corresponding to the main coolant system was kept at an arbitrary pressure from atmospheric pressure to 0.5 MPaG. The accumulator tank was initially supplied with water and then nitrogen gas to a given pressure before every test.

Since the pressure in the accumulator tank was the same as the actual one, the velocity of flow in the flow damper was the same as that in the actual damper under the corresponding conditions. The flow damper and outlet pipe were half-scale. The diameters of the accumulator tank and the standpipe were also half-scale, but their heights were full-scale so that the transitions of water levels were the same as the

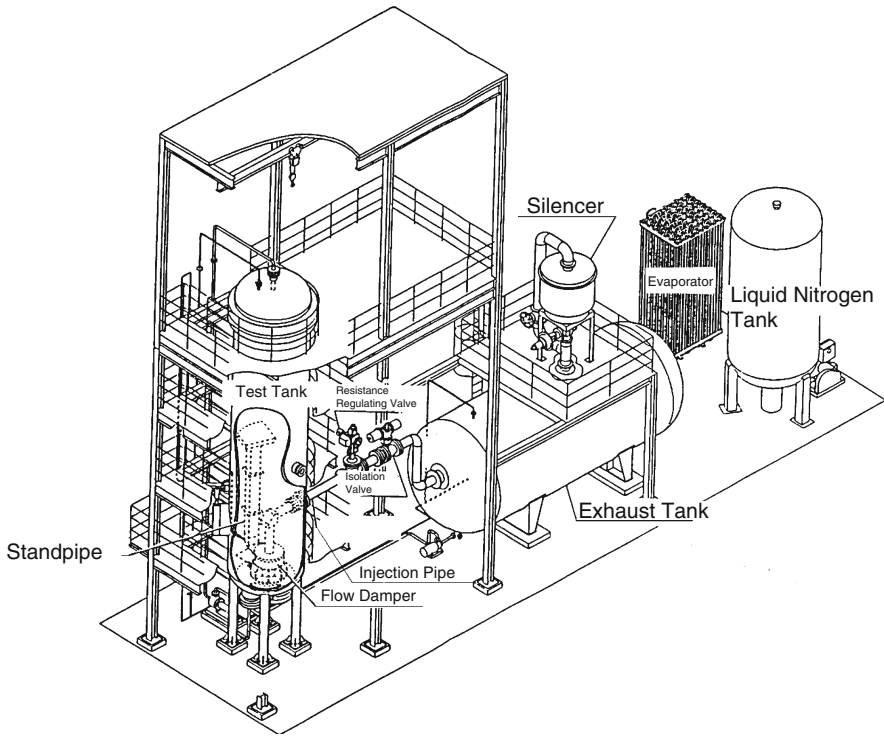


Fig. 2.36 A cut-away view of the test facility of the full-height 1/2-scale model of the Advanced Accumulator under the actual pressure conditions. The flow damper was installed at the bottom of the test tank. It could simulate the entire integrated functions of the Advanced Accumulator with the real time injection of flow

actual ones under the actual pressure conditions. Consequently, the time scale was also the same as the actual one.

The objectives of the tests were:

1. Confirmation of the expected performance
2. Confirmation of the flow rate characteristics
3. Assessment of the water level at flow changeover
4. Assessment of the influence of dissolved nitrogen gas.

It was expected that the principle confirmed by the 1/8.4-scale model would be implemented without any unexpected problem in the large-scale accumulator under the actual pressure conditions in the sequence of the large flow injection, change-over of flow rates, and small flow injection.

The flow rate characteristics, which were obtained by the half-scale model under the actual pressure conditions, should be compared with those obtained by the 1/5-scale model. If they agree with each other, it can be concluded that the Reynolds numbers will negligibly affect the characteristics of the flow damper.

Then, the characteristics of the half-scale model of the Advanced Accumulator will be adoptable to the full-scale accumulator.

The water level at flow changeover is important to secure the total volume and the duration of large flow injection. Since the descending velocity of the water level in the model tank of the accumulator is the same as that in the actual Advanced Accumulator, assessment of the accuracy of the water level at the flow changeover will be reliable.

For the evaluation of the influence of dissolved nitrogen gas, the water in the test tank was saturated with nitrogen gas before the tests. There were a ring header at the bottom of the test tank to emit nitrogen bubbles underwater and a spray nozzle at the top of the test tank to spray water into the gas space. The water for the spray was pumped up by a circulation pump as shown in Fig. 2.37.

The pressure in the test tank was monitored while bubbling gas and spraying water. The pressure first decreased due to dissolution of nitrogen gas into water, and later approached a constant value when water became saturated with nitrogen. Nitrogen gas was supplied to the test tank until the pressure became unchanged at the given value. It took about 3 or 4 h to get saturation in this test tank. After confirming the pressure became stable, the bubbling and the spraying were stopped. Hence, the water would not only be saturated with nitrogen but would also contain many cavitation nuclei. It must be much easier for cavitation to occur for this condition of the water than the condition of borated water in the actual accumulator tank.

Pressures in the test tank, the injection pipe and the exhaust tank were measured with pressure transducers. Water levels in the test tank and the standpipe were

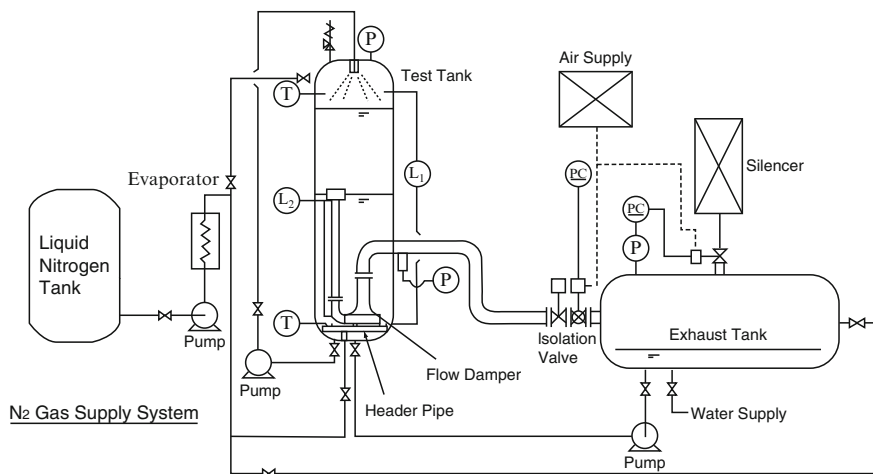


Fig. 2.37 Schematic of the test facility. Nitrogen gas was supplied from the liquid nitrogen tank through the evaporator not only for pressurization of the test facility, but also for dissolution of nitrogen gas into water. The ring header provided bubbling at the bottom of the test tank and the spray nozzle provided a water spray from the circulation pump. Quantities measured were pressures in the test tank, the injection pipe, and the exhaust tank, water levels in the test tank and the standpipe, and temperatures in the test tank

measured with a differential pressure transducer and an electrocapacitance level meter, respectively. The flow rates were calculated from the water level in the test tank. Temperatures in the test tank were measured with thermocouples.

Figure 2.38 shows an example of the test results in Case 1 obtained by the full-height 1/2-scale model. Figure 2.38a shows the transitions of water levels in the test tank and the standpipe, which were identical to those of the actual accumulator. The water level in the test tank rapidly decreased to the top of the standpipe for large flow injection, and slowly decreased for small flow injection thereafter. When the water level in the test tank reached the top of the standpipe, the water level appeared in the standpipe and plummeted to form the undershoot. The water level then recovered to the balanced level and slowly decreased as the water level in the test tank slowly descended.

Figure 2.38b shows the transitions of flow rate of the test calculated from the gradient of the transition of the water level in the test tank. The actual flow rate expected was four times this flow rate. Quick changeover of the flow rate was clearly seen. The decrease for large flow injection was caused by the pressure drop in the test tank due to the expansion of nitrogen gas.

Figure 2.38c shows the transitions of pressures in the test tank and the injection pipe, which were identical to those of the actual accumulator. Pressure rapidly fell once the injection started. The pressure in the injection pipe quickly changed at the changeover of flow rate, and became the same as that in the exhaust tank.

The flow-rate characteristics of the flow damper in Case 1 are shown in Fig. 2.39. The data were divided into two groups for large and small flow injections. The flow rate coefficient depended on the cavitation factor for large flow injection, while it was independent of the cavitation factor for small flow injection. These data agreed with those obtained by the 1/5-scale model of the flow damper shown in Fig. 2.35. Therefore, it could be concluded that the flow rate characteristics of the flow damper were independent of Reynolds numbers, and these data obtained by the full-height 1/2-scale model would be applicable to the actual flow damper. Care should be taken that, if the flow damper was small in size and the Reynolds number was small, viscosity of the fluid might affect its characteristics.

We considered a nitrogen bubble in saturated water with nitrogen that experiences abrupt depression from the storage pressure to atmospheric pressure at time $t = 0$ s in a stepwise manner in order to examine the growth of the bubble. The bubble at first rapidly expands due to gas expansion then nitrogen slowly permeates in water due to diffusion of saturated nitrogen. Bubble dynamics due to gas expansion in inviscid fluid is given by (2.23) [12]

$$P(t) = p_0 + \frac{1}{2}\rho \left[\frac{d^2(R^2)}{dt^2} + \left(\frac{dR}{dt} \right)^2 \right], \quad (2.23)$$

where R is the radius of the bubble; $P(t)$ is pressure on the surface of the bubble; t is time; ρ is the density of the fluid; and p_0 is the ambient pressure.

The distension of a spherical bubble with an initial radius of 0.05 mm due to gas expansion is shown in Fig. 2.40. The surface tension on the bubble was taken into

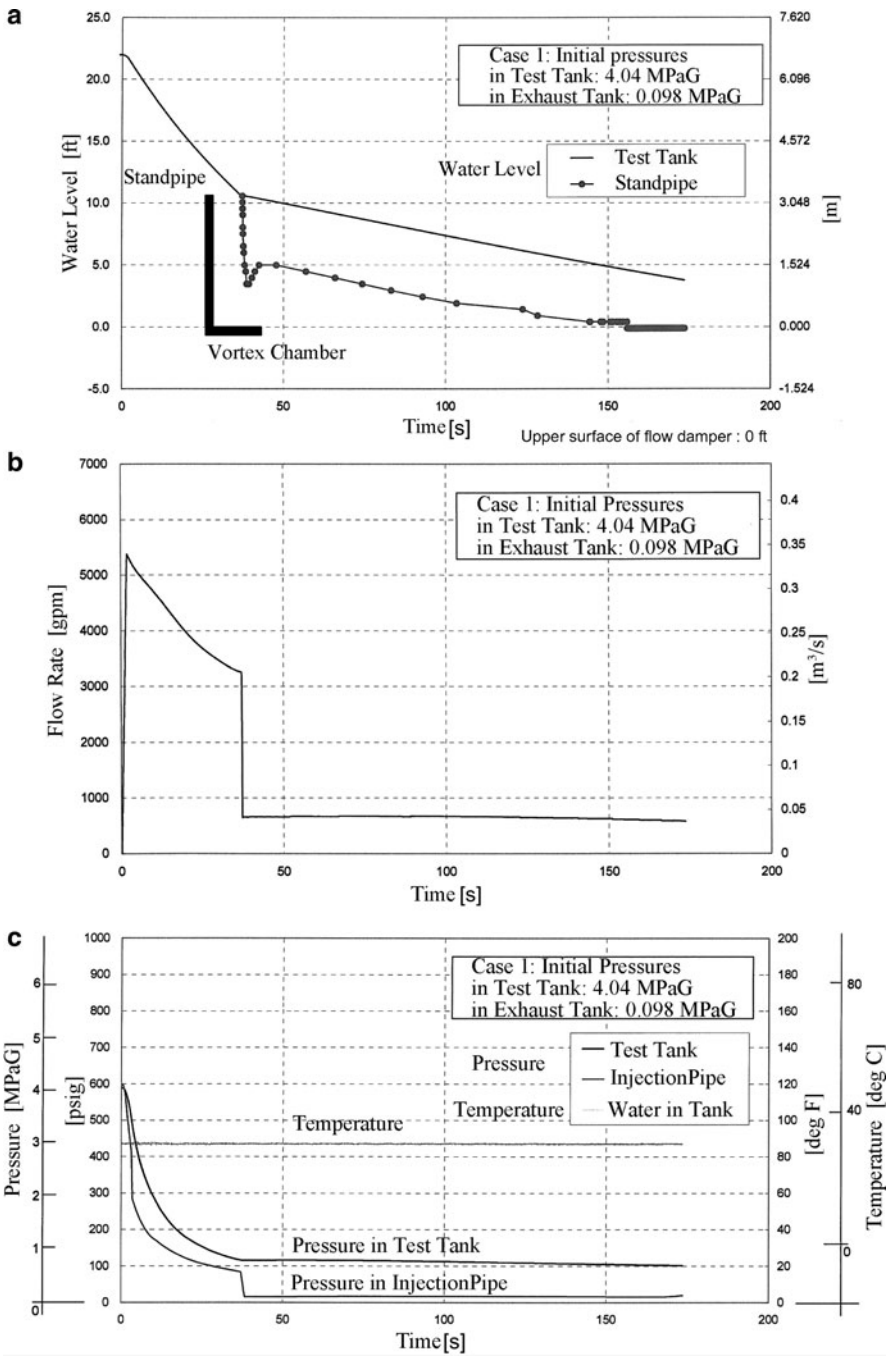


Fig. 2.38 An example of transitions of water levels in the test tank and the standpipe

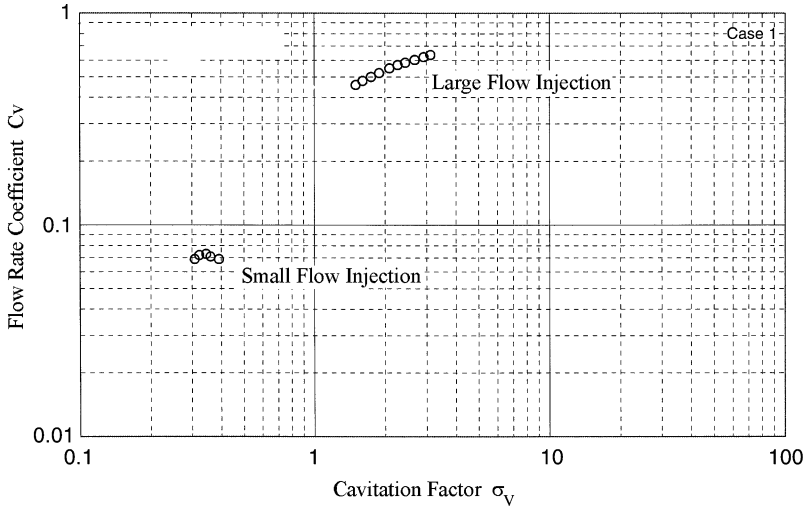


Fig. 2.39 An example of flow rate characteristics in Case 1 obtained by the full-height 1/2-scale model. The flow rate coefficient was clearly divided into two groups for large and small flow injections, the same as for the data obtained by the 1/5-scale model in Fig. 2.35. These data agreed well with each other

account in the calculation. Bubble distension due to gas expansion was very rapid. For the adiabatic change, or the specific heat ratio $\gamma = 1.4$, the bubble was distended in 9×10^{-6} s, and for the isothermal change, or $\gamma = 1.0$, the bubble was distended in 1.6×10^{-5} s. An actual bubble would be abruptly distended within a time between these times.

Nitrogen diffusion slowly affects the growth of a bubble. For simplicity, the solution of one-dimensional diffusion of nitrogen in the water around a bubble is given as:

$$c = c_R + (c_\infty - c_R) \operatorname{erf} \frac{x}{2\sqrt{Dt}}, \quad (2.24)$$

where c is concentration of nitrogen, c_R and c_∞ are concentrations at radii $r = R$ and $r \rightarrow \infty$, respectively. $x = r - R$. D is the diffusion coefficient of nitrogen in water, and an error function is

$$\operatorname{erf} \eta = \frac{2}{\sqrt{\pi}} \int_0^\eta \exp(-\xi^2) d\xi. \quad (2.25)$$

The distension of the spherical bubble due to nitrogen diffusion after the gas expansion is shown in Fig. 2.41. Henry's law was applied to calculate the balance of pressure in the bubble and density of nitrogen in water around the bubble.

It was shown that the distension due to the diffusion of nitrogen was very slow, and the growth of the bubble was small for about 0.15 s which is the time for a bubble

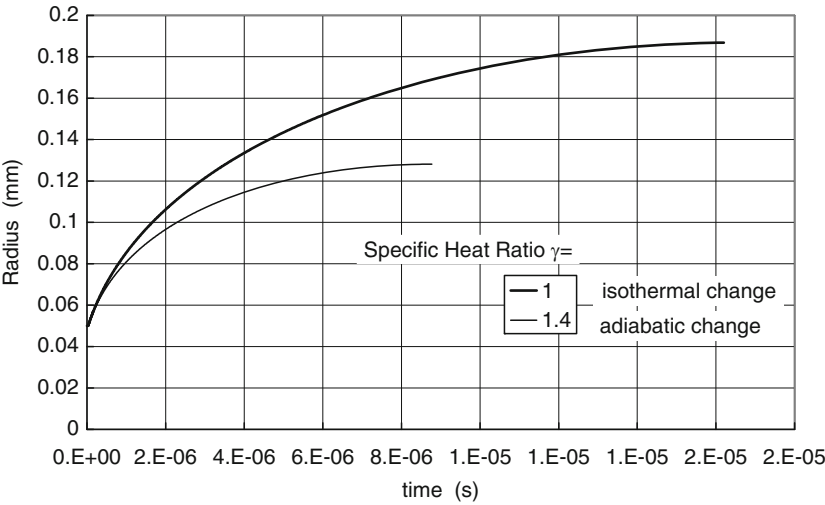


Fig. 2.40 Examples of distensions of a nitrogen bubble due to gas expansion are shown for specific heat ratios $\gamma = 1$ and 1.4, namely isothermal and adiabatic changes, respectively. Both distensions finished in 2×10^{-5} s

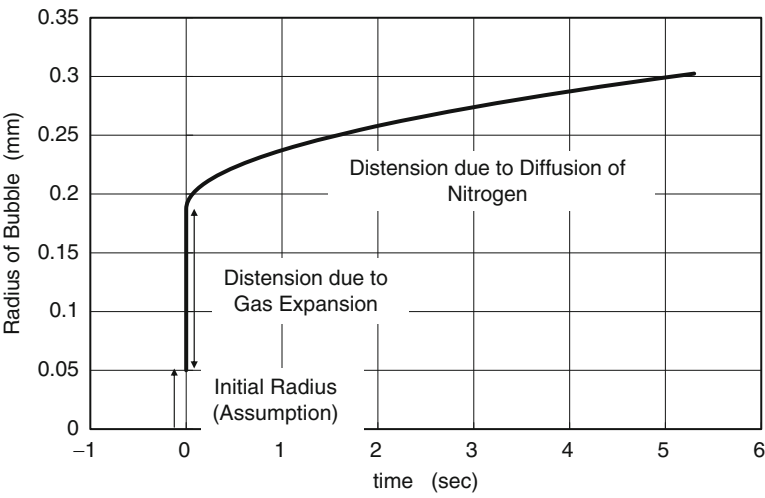


Fig. 2.41 An example of distension of a nitrogen bubble due to diffusion after the adiabatic gas expansion. This distension was the order of 1 s and much slower than that due to the gas expansion shown in Fig. 2.40

in water to pass through the vortex chamber and the throat. The diffusion around a bubble depends on its radius and is nonlinear. But the diffusion of nitrogen in this case was also very slow.

The speed of nitrogen diffusion was the same for cavitation nuclei on the walls as for bubbles in water. The former were sedentary on the walls and the bubbles expanded to a certain size at which superjacent flow carried them away. The growth rate would be controlled by slow diffusion of nitrogen in water.

Consequently, the effect of nitrogen was seen in the abrupt distension of bubbles, or cavitation nuclei, in the form of gas expansion in the accumulator tank, and diffusion of nitrogen was negligible in the flow damper. This investigation about the effect of dissolved nitrogen was confirmed by the full-height 1/2-scale tests.

As results of the full-height 1/2-scale tests, we saw the following:

1. The flow rate coefficient decreased as cavitation factor got smaller for large flow injection.
2. The flow rate coefficient approached a constant value as cavitation factor got larger for large flow injection.
3. The flow rate coefficient was independent of a cavitation factor for small flow injection.

Finding 1 was reasonable because cavitation was stronger for a smaller cavitation factor. Finding 2 was reasonable because cavitation vanished for a large cavitation factor. Finding 3 was reasonable because flow rate was small, and the pressure at the throat was almost the same as that in the exhaust tank which was larger than the vapor pressure.

Consequently, the Advanced Accumulator has been developed, and is going to be adopted for the APWR.

2.7 Structure of Flow in the Flow Damper

To understand the structure of flow in the flow damper, we carried out computational analysis with a commercial code, Fluent Ver.6.2.16 (developed by Fluent Inc.) [13]. Our problem was to investigate the flow characteristics in the flow damper for small flow injection using steady flow analysis of incompressible single-phase viscous fluid. Cavitation was not included in this case. The turbulence model applied was the Reynolds Stress Model. The wall function was used to solve the flow near solid wall boundaries. The second-order upwind finite difference scheme was used for the equation of motion, and the first-order upwind finite difference scheme was used for the others.

Figure 2.42 shows an example of the flow pattern visualized by tracers for small flow injection at the nominal condition. A combined vortex of a free vortex with a forced vortex at the center of it was formed in the vortex chamber and rapidly decreased in the reducer. The maximum velocity reaches 40 m/s in the combined vortex. There was a weak circulating flow induced in the stand pipe. The vortex became a swirl in the reducer and entered the diffuser. The swirl further decreases in the diffuser. Since the swirl flowed along the wall of the diffuser and a backflow was induced on the axis of the diffuser, it transported pressure from the injection

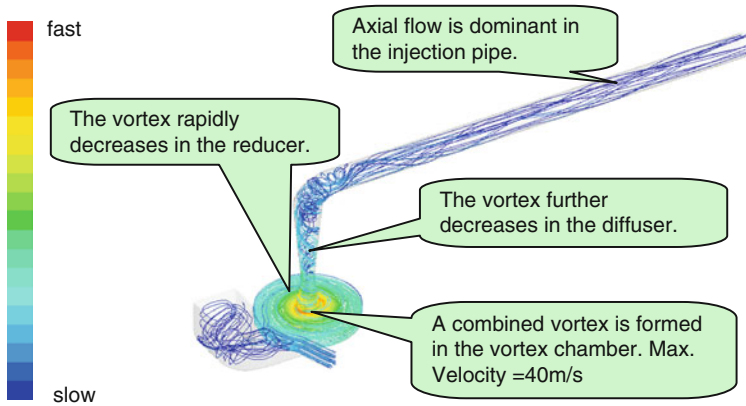


Fig. 2.42 The flow pattern for small flow injection. The vortex formed in the chamber rapidly decreases in the outlet nozzle, and a small swirl remains in the injection pipe

pipe to the throat. The backflow kept the pressure at the throat close to that in the injection pipe. The axial flow was dominant in the injection pipe, and the swirl flow vanished. The structure of the flow was just what we expected.

Figure 2.43 shows an example of the total pressure distribution for small flow injection at the nominal condition. Total pressure was conserved in the free vortex region and 90% of the total pressure was lost by shear stress at the vortex core in the chamber and the reducer. The rest of the total pressure was lost by turbulent shear stress in the diffuser. The pressure loss was slight in the injection pipe.

Now, we were able to see the mechanism of the flow damper. In the vortex chamber, static pressure was converted to dynamic pressure to form a strong swirl with very high velocity. But, the total pressure was conserved. The high velocity of the swirl yielded high shear stress at the center of the swirl so that the most of the total pressure was lost in the reducer. The remaining weak swirl was also lost by turbulent shear stress in the diffuser to form an axial flow in the injection pipe. Consequently, the vortex chamber converted static pressure to dynamic pressure and energy loss was produced at the center of the vortex chamber and in the outlet nozzle.

Figure 2.44 shows the distributions of the total pressure and the turbulent energy in the vertical cross section of the flow damper. Figure 2.44a indicates a free vortex was formed in the vortex chamber at the center of which there was minimum total pressure. The boundary layers on the upper- and lower-disk walls of the vortex chamber were very thin, and the inviscid flow prevailed in the chamber, except at its center near the outlet port. It ensured two dimensionality of the vortex flow in the chamber and independency of the flow rate characteristics of the flow damper from Reynolds numbers. The location of the minimum total pressure corresponded to the location of the minimum static pressure. If the velocity was very high, cavitation might occur and be confined there by the reducer. The total pressure plummeted in

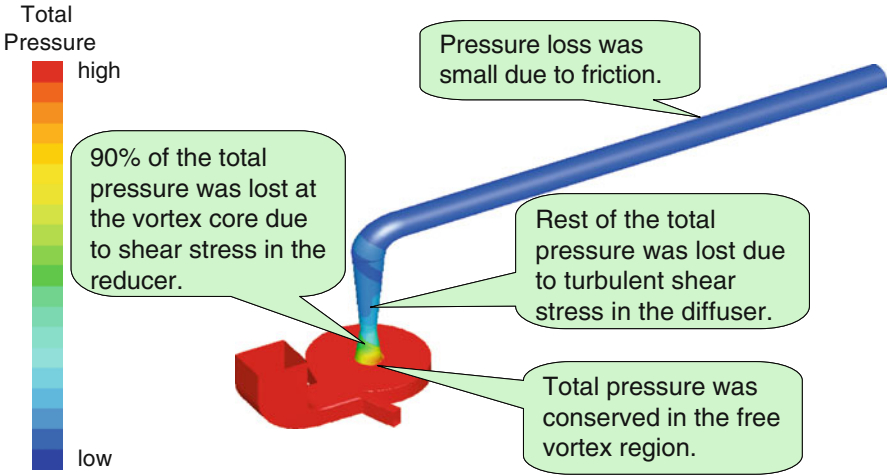


Fig. 2.43 The total pressure distribution for small flow injection. A free vortex is formed in the vortex chamber except in the vortex core and 90% of the total pressure is lost by the shear stress at the vortex core in the chamber and the reducer

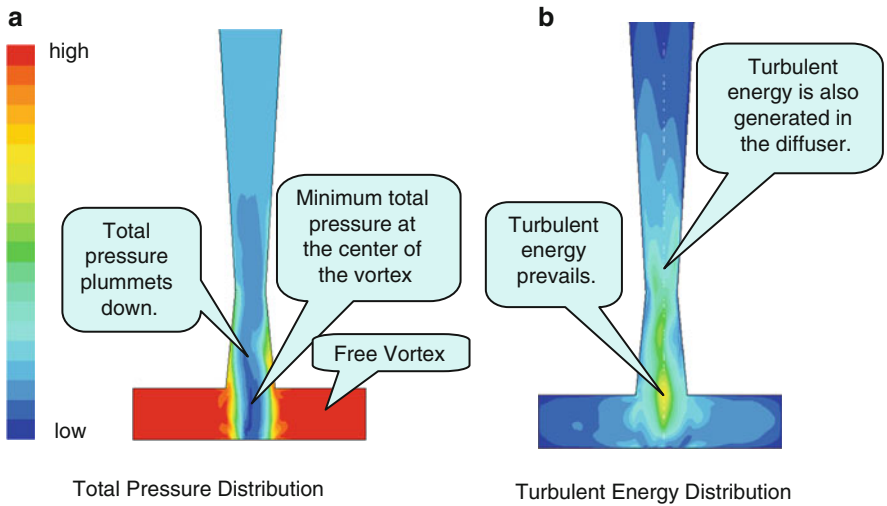


Fig. 2.44 Distributions of the total pressure and the turbulent energy in the vertical cross section of the flow damper. It was clear that total pressure was conserved in the vortex chamber to form a free vortex except in the vortex core. Turbulent energy prevailed at the vortex core

the reducer. But, the backflow on the axis of the diffuser recovered the pressure at the throat close to that in the injection pipe.

Figure 2.44b indicates the turbulent energy prevailed at the core of the swirl on the centerline of the vortex chamber and in the reducer. It was produced by shear stress. Turbulent energy was also generated in the diffuser just after the throat due

to reduced velocity of flow. The pattern of the turbulent energy in the diffuser was made by the swirl near the wall and the backflow at the center.

2.8 Conclusion

Mitsubishi has developed a new passive safety component for the APWR called the Advanced Accumulator, which uses a fluidics device called the flow damper. It can control flow rate without any moving parts so that the reliability of the Advanced Accumulator is very high. The background of the development and the features of the Advanced Accumulator are explained in this chapter. The characteristics of the flow damper are investigated in detail and some results are introduced here. The structure of flow in the flow damper is also explained.

Acknowledgments We acknowledge the five Japanese utilities, Hokkaido Electric Power Co., Kansai Electric Power Co., Shikoku Electric Power Co., Kyushu Electric Power Co., and Japan Atomic Power Company, for their understanding and encouragement to develop the Advanced Accumulator. We thank many supporters and cooperators, especially Mr. Hisato Watakabe for his excellent skills for carrying out all the experiments to develop the Advanced Accumulator, and Mr. Takayoshi Sugizaki for his distinguished management of the development.

References

1. Suzuki S et al (2008) Global development of Mitsubishi standard APWR as an effective countermeasure against global warming. Mitsubishi Heavy Industries Technical Review 45(3)
2. Makihara Y et al (1993) Study of the PWR hybrid safety system. Nucl Eng Des 144:247–256
3. Shiraishi T (1994) Emergency water supply system for nuclear reactor. Japanese Patent H6-44060
4. Shiraishi T et al (1991) On flow controlled accumulator for Mitsubishi's simplified PWR (MS-300/600). Proc JSME B (in Japanese)
5. Shiraishi T et al (1992) Development of the flow controlled accumulator. ANP'92, Tokyo
6. Sugizaki T et al (1992) Design Studies for a passive safeguards system. NURETH-5
7. Shiraishi T et al (1994) Assessment of the performance of the flow controlled accumulator for next generation PWR. Proc JSME B (in Japanese)
8. Shiraishi T et al (1994) Characteristics of the flow-controlled accumulator. Nucl Technol 108:181–190
9. Shiraishi T et al (1994) Development of the advanced accumulator for next generation PWR. Therm Nucl Power Eng 45(6):43–49 (in Japanese)
10. Shiraishi T et al (1994) Development of the advanced accumulator. Mitsubishi Heavy Industries Technical Review 31(1)
11. Shiraishi T (1997) Flow control by a vortex (flow damper). Turbo Mach 25(9):54–61 (in Japanese)
12. Landau LD, Lifshitz EM (1975) Fluid mechanics. Pergamon Press, Oxford
13. Takata T et al (2009) CFD on small flow injection of advanced accumulator in APWR. Mitsubishi Heavy Industries Technical Review, 46(2)

Advances in Light Water Reactor Technologies

Saito, T.; Yamashita, J.; Ishiwatari, Y.; Oka, Y. (Eds.)

2011, XIV, 295 p., Hardcover

ISBN: 978-1-4419-7100-5